

The Spectral Components of SS 433

D. R. Gies^{1,2}, M. V. McSwain^{1,2}, R. L. Riddle^{1,2,3}, Z. Wang^{1,4}, P. J. Wiita⁵, D. W. Wingert¹

Center for High Angular Resolution Astronomy

Department of Physics and Astronomy

Georgia State University, Atlanta, GA 30303

*Electronic mail: gies@chara.gsu.edu, mcswain@chara.gsu.edu, riddle@iastate.edu,
wangzx@space.mit.edu, wiita@chara.gsu.edu, wingert@chara.gsu.edu*

ABSTRACT

We present results from new optical and UV spectroscopy of the unusual binary system SS 433, and we discuss the relationship of the particular spectral components we observe to the properties of the binary. These spectral components include:

(1) The continuum spectrum which we associate with flux from the super-Eddington accretion disk and the dense part of its wind. A FUV spectrum from HST/STIS made during the edge-on orientation of the disk places an upper limit on the temperature of an equivalent blackbody source ($T < 21,000$ K for $A_V = 7.8$) when combined with NUV and optical fluxes. The continuum source has a radius of approximately half the binary separation which may be larger than the Roche radius of the compact star.

(2) H α moving components which are formed far from the binary orbital plane in the relativistic jets. We confirm that these emission features appear as “bullets” at a fixed wavelength and may last for a few days. We present a contemporary

¹Visiting Astronomer, Kitt Peak National Observatory, National Optical Astronomy Observatories, operated by the Association of Universities for Research in Astronomy, Inc., under contract with the National Science Foundation.

²Visiting Astronomer, University of Texas McDonald Observatory.

³Current Address: Department of Physics and Astronomy, Iowa State University, Ames, IA 50011

⁴Current address: Center for Space Research, Massachusetts Institute of Technology, 70 Vassar Street, Building 37, Cambridge, MA 02139

⁵On leave at Department of Astrophysical Sciences, Princeton University

radial velocity curve for the precessional motion of the jets which includes the nodding motion caused by tidal interaction with the optical star.

(3) $H\alpha$ and He I “stationary” emission lines which we suggest are formed in the disk wind in a volume larger than the dimensions of the binary. These lines vary on all time scales and sometimes appear as P Cygni lines. We suggest that their radial velocity curves (which show greatest redshift at inferior conjunction of the optical star) result from an evacuation of the disk wind surrounding the optical star (caused by physical blockage, heating, or colliding winds). We argue that the wake of this interaction region causes an extended eclipse of the X-ray source (as seen in RXTE/ASM light curves).

(4) A weak “stationary” emission feature we identify as a C II $\lambda\lambda 7231, 7236$ blend that attains maximum radial velocity at the orbital quadrature of disk recession (like the velocity curve of He II $\lambda 4686$). This is probably formed in outflow from the central region of the disk near the compact star.

(5) Absorption and emission features from outflowing clumps in the disk wind (seen most clearly in an episode of blue-shifted Na I emission).

(6) We found no clear evidence of the absorption line spectrum of the optical star, although we point out the presence of He I absorption features (blended with the stationary emission) with the expected radial velocity trend at the orbital and precessional phases when the star might best be seen.

(7) A rich interstellar absorption spectrum of diffuse interstellar bands.

The results suggest that the binary is embedded in an expanding thick disk (detected in recent radio observations) which is fed by the wind from the super-Eddington accretion disk.

Subject headings: binaries: spectroscopic — stars: early-type — stars: individual (SS 433; V1343 Aql) — stars: winds, outflows

1. Introduction

The unusual binary system, SS 433, is both of one of the most famous and still most mysterious of the X-ray binary systems (van den Heuvel 1981; Margon 1984; Clark 1985; Zwitter et al. 1989). The basic scenario that has emerged from 24 years of investigation is of an evolved binary caught in the act of extensive mass transfer. The mass donor feeds an enlarged accretion disk surrounding a neutron star or black hole companion, and some of the mass inflow is redirected through the influence of the disk into oppositely directed relativistic jets that are observed in optical and X-ray emission lines and in high resolution

radio maps. There are two basic clocks that dominate the spectral appearance and system dynamics. The first is a 162 d periodicity that is observed in the extreme radial velocities of the “moving” set of emission lines. These red and blue, mirror-symmetry motions are well described by the “kinematical model” of emission from jets driven by a precessing disk (Fabian & Rees 1979; Milgrom 1979a; Abell & Margon 1979).

The second clock is the 13 d orbital period itself which was first discovered through the radial velocity variations of a set of “stationary” emission lines that presumably originate in or near the disk (Crampton et al. 1980; Crampton & Hutchings 1981). The H Balmer and He I lines reach maximum velocity at superior conjunction of the X-ray source, and so this emission could originate in a gas stream from donor to compact star. However, the high excitation emission line He II $\lambda 4686$ has a different radial velocity curve with a maximum occurring at the quadrature when the compact object is receding (Crampton & Hutchings 1981; Kopylov et al. 1989; D’Odorico et al. 1991; Fabrika 1997). This suggests that the He II $\lambda 4686$ radial velocity curve traces the orbital motion of hot gas near the compact star. The orbital mass function indicates that the donor star mass is in excess of $8 M_{\odot}$ (Fabrika 1997), so we expect that the surviving star is a massive OB object (although the clear spectral signature of this star has eluded detection).

The other major periodicity found in the radial velocities of the jets, 6.28 days, corresponds to the time between the star’s passage through the nodal line of the disk, and this results from recurrent tidal deformations or “nodding” of the disk. Thus, the combination of the precessional and orbital periods has provided a very successful description of the jet motions (Katz et al. 1982; Collins & Garasi 1994) and the photometric variations (Goranskii et al. 1998a). Nevertheless, there remain a number of outstanding puzzles: the actual masses and nature of the donor and collapsed stars (Fukue et al. 1998), the jet formation process (Panferov 1999; Okuda & Fujita 2000; Inoue et al. 2001), the origin of the disk precession (Wijers & Pringle 1999; Ogilvie & Dubus 2001), and the evolutionary state of the binary (King et al. 2000).

The optical continuum spectrum of SS 433 has the shape of a highly reddened, Rayleigh-Jeans distribution implying an origin in a hot object (Murdin et al. 1980; Cherepashchuk et al. 1982; Wagner 1986; Dolan et al. 1997). The optical flux varies on the same precessional cycle as the jets (Goranskii et al. 1998a) and results from the changing orientation of the precessing disk (Leibowitz 1984; Antokhina & Cherepashchuk 1987; Fukue et al. 1998). The large amplitude of the precessional variation indicates that the disk is the dominant flux source in the optical band. The system also displays an orbital light curve with two unequal eclipses (Goranskii et al. 1998a), and the primary eclipse occurs when the X-ray source is eclipsed (Stewart et al. 1987). The relative depths of the eclipses indicate that the disk

source has a characteristic temperature twice that of the optical star (Cherepashchuk et al. 1982; Leibowitz 1984; Antokhina & Cherepashchuk 1987). Models of the optical light curve favor a mass ratio $q = M_X/M_O = 0.4$ to 1.2 (Antokhina & Cherepashchuk 1987; Fukue et al. 1998) which suggests a massive black hole companion, while models of the X-ray light curve (Antokhina et al. 1992) indicate a smaller mass ratio indicative of a neutron star companion. This dilemma could be solved if the spectrum of the companion could be identified and its orbital velocity curve measured to provide a direct determination of the mass ratio.

The other important observational challenge is to explore the faint ultraviolet part of the spectrum so as to better determine the temperature of the hot, super-Eddington disk and the nature of its UV radiation field which could play an important role in the mass outflow (Milgrom 1979b; Panferov 1999). Dolan et al. (1997) succeeded in observing SS 433 in the near-UV with the High Speed Photometer aboard the *Hubble Space Telescope*. Their work shows that the continuum polarization rises steeply towards the UV. They sought but found no evidence of rapid flux variability in the UV that might be associated with the spin period of the collapsed star. Unfortunately, their flux measurements at 2770 Å are still far removed from the Wien peak of the expected flux distribution, and large uncertainties remain about the temperature associated with the continuum light. For example, Dolan et al. (1997) fitted the optical and near-UV fluxes with a blackbody spectrum with $T = 72,000$ K and $A_V = 8.4$ while Wagner (1986) fitted optical spectrophotometry with $T = 45,000$ K and $A_V = 7.8$ (in both cases for the spectrum observed near photometric maximum when the disk normal is closest to our line of sight and the disk face attains its largest projected area on the sky).

Here we describe our recent program of spectroscopy of SS 433 designed to answer some of these outstanding issues. We first discuss a program of extensive, moderate resolution, optical spectroscopy obtained with the Kitt Peak National Observatory Coude Feed Telescope and the University of Texas McDonald Observatory 2.1-m Telescope between 1998 - 1999 (§2). The properties of the jet lines are described in §3, and the stationary lines are discussed in §4. We examine in §5 the continuum spectrum in the vicinity of H α to search for evidence of the optical companion. We describe the first observation of the far-UV spectrum of SS 433 with the *Hubble Space Telescope* Space Telescope Imaging Spectrograph in §6. Finally, we summarize in §7 the observed spectral components of SS 433 and their interpretation in framework of the binary model, along the same lines as done in earlier work by Murdin et al. (1980) and Cherepashchuk et al. (1982).

2. Optical Spectroscopy

The optical spectra were obtained mainly with the Kitt Peak National Observatory 0.9-m Coude Feed Telescope between 1998 August and 1999 November. A summary of the different observing runs is given Table 1 which lists the beginning and ending heliocentric dates of observation, the wavelength range recorded, the spectral resolution ($\lambda/\delta\lambda$), the number of spectra, and the instrumental configuration (codes for the observatory, telescope, grating, and detector). In the most common configuration with the Coude Feed, we used the short collimator, grating RC181 (in first order with a GG495 filter to block higher orders), and camera 5 with a Ford 3072×1024 CCD (F3KB) as the detector. We set the grating at two tilts to cover fully the wavelength range of the $H\alpha$ jet features in SS 433 (5900 – 7750 Å). There were several departures from this standard arrangement. The detector on the first night of the 1999 observations was a Texas Instruments 800×800 CCD (TI5), and we only recorded the spectrum with one grating setting in the immediate vicinity of the rest $H\alpha$ line. The somewhat higher dispersion spectra from 1998 were made using the long collimator, grating B (in second order with order sorting filter OG550), camera 5, and the F3KB CCD. Only one grating setting was used, and thus the wavelength range is limited. Finally, we also obtained several high dispersion echelle spectra of SS 433 using the University of Texas McDonald Observatory 2.1-m telescope and Sandiford Cassegrain Echelle Spectrograph (McCarthy et al. 1993). The detector was a Reticon 1200×400 CCD (RA2) with $27\mu\text{m}$ square pixels which recorded 27 echelle orders covering the region blueward from $H\alpha$.

We usually obtained two consecutive exposures of 30 minutes duration and co-added these spectra to improve the S/N ratio. We also observed with each configuration the rapidly rotating A-type star, ζ Aql, which we used for removal of atmospheric water vapor and O_2 bands. Each set of observations was accompanied by numerous bias, flat field, and Th Ar comparison lamp calibration frames.

The spectra were extracted and calibrated using standard routines in IRAF⁶. The Coude Feed spectra were traced, extracted (after subtraction of the sky background), and wavelength calibrated using the IRAF routine *doslit*, and the same tasks were done using *doecslit* for the McDonald Observatory Sandiford echelle spectra. The blaze function response of the echelle spectra was removed by division of fits to spectra of hot single stars (or in some cases by fits of the flat field spectra). All the spectra were rectified to a unit continuum by

⁶IRAF is distributed by the National Optical Astronomy Observatories, which is operated by the Association of Universities for Research in Astronomy, Inc., under cooperative agreement with the National Science Foundation.

the fitting of line-free regions using the IRAF task *continuum* (and in the case of the echelle spectra, the resulting orders were then linked together using the task *scombine*). Note that the rectification process arbitrarily removes the continuum flux variations that are known to exist in the spectrum of SS 433, and the intensities of the emission lines must be interpreted bearing in mind this renormalization. The removal of atmospheric lines was done by creating a library of ζ Aql spectra from each run, removing the broad stellar features from these, and then dividing each target spectrum by the modified atmospheric spectrum that most closely matched the target spectrum in a selected region dominated by atmospheric absorptions. We also removed the most obvious air glow emission lines at this stage. The spectra from each run were then transformed to a common heliocentric wavelength grid. Finally, we transformed the spectra from all the runs onto a standard $\log \lambda$ wavelength grid between 5400 and 7793 Å with a grid spacing equivalent to 20 km s⁻¹ (this binning operation effectively lowered the resolution but increased the S/N of the echelle spectra).

3. Moving Emission Lines

We begin by describing the appearance in our spectra of the “moving” components of H α which originate in the relativistic jets of SS 433 (Vermeulen et al. 1993a; Panferov et al. 1997). Our primary motivation is twofold: to establish an accurate velocity curve for the precessional cycle during our observations and to identify those times when the moving components cross and blend with the “stationary” lines. Figure 1 shows the spectral regions that included the moving lines during our final run when the moving components were both strong and unblended with the stationary lines. The left panel represents the nightly progression in the components from the approaching jet (H α -) while the right panel shows the receding jet components (H α +). Our results confirm the conclusions of Borisov & Fabrika (1987), Vermeulen et al. (1993a), and others that these jet components appear as distinct “bullets” of emission that appear suddenly at specific wavelengths and then decline on a time scale of a few days at the same position. There is often (but not always) a correspondence between the Doppler shifts and strengths of components from the approaching and receding jets. We also confirm the dramatic variations in the intensities of the moving line components (Kopylov et al. 1986, 1987); for example, there were four nights near HJD 2,451,426 when any jet components were weaker than our detection threshold (intensity < 6% of the continuum). We inspected the individual spectra for evidence of moving components of He I $\lambda\lambda$ 5876, 6678, 7065 (which have significant stationary lines), and weak but plausible emission components were only found in cases where the H α moving emission components were relatively strong.

Following the approach of Vermeulen et al. (1993a), we found that the only practical method of measuring the Doppler shifts of these components was to make Gaussian fits of each clearly evident emission peak (using the IRAF routine *splot*). There are several cases where the emission profiles significantly depart from a Gaussian shape (probably due to blending of several components), and we used multiple Gaussian fits in those cases where an obvious intensity minimum separated neighboring peaks. Our measurements of Doppler shift, z , equivalent width, W_λ , and profile full width at half maximum, FWHM, are listed in Table 2. The measured z values are plotted against time in Figure 2.

The radial velocity curve displays the well-known 162 d precessional variation plus shorter term “nodding” motions that were first discussed by Katz et al. (1982). Katz et al. (1982) show that a disk inclined to the orbital plane will experience gravitational torques caused by the orbiting star that will vary with the nutational period, $(2P_{\text{orb}}^{-1} + P_{\text{prec}}^{-1})^{-1}$, where P_{orb} and P_{prec} are the orbital and precessional periods. This 6.28 d nodding motion dominates in the measurements from individual observing runs. We decided to fit our z measurements using the Katz et al. (1982) model as a simple means to parameterize the complicated velocity curves. Although more sophisticated models are available (Collins & Garasi 1994), their use was not warranted given the limited data available and the basic uncertainties surrounding the origin of the precessional motion (Wijers & Pringle 1999).

We decided to constrain the fit at the outset with three well-determined parameters set according to the results of Margon & Anderson (1989) based upon observations spanning a decade: jet velocity, $v/c = 0.2602$, precessional angle between the jet and orbital plane normal, $\theta_0 = 19^\circ.85$, and inclination of precessional axis, $i = 78^\circ.83$. We took the precessional period, $P_{\text{prec}} = 162.15$ d, and the orbital period, $P_{\text{orb}} = 13.08211$ d, from the extensive photometric light curve results of Goranskii et al. (1998a). We then made a non-linear least squares solution for the three remaining parameters in the Katz et al. (1982) model: t_{or} , the epoch of a time of binary quadrature, ξ_0 , the angle of the disk line of nodes to the line of sight at time t_{or} , and $P_0 = 2\pi/\Omega_0$, a parameter that sets the semiamplitude of nodding perturbation motions in θ and ξ (the azimuthal angle). We applied weights to each measurement for fitting purposes of $1/(\Delta z)^2$ where we estimated a Doppler shift error of $\Delta\lambda(\text{\AA}) \approx 0.05 + 7/|W_\lambda|$ from measurements in consecutive spectra. This effectively weights the solution in favor of the strongest emission components present. We arbitrarily selected a time close to the radial velocity extrema of the jet components as a starting value for t_{or} . Our fitting results are summarized in Table 3 where we list the number of jet measurements used (N), epoch (t_{or}) for the angle to the line of nodes (ξ_0), the semiamplitude of the nodding motion in the azimuthal direction ($\Delta\xi$; the semiamplitude in the θ direction is $0.36\Delta\xi$), and the root-mean-square deviation in z of the fit (which is much larger than the measurement errors or indeed the widths of the emission components; see Fig. 6 below). The results from

the $H\alpha-$ and $H\alpha+$ measurements are negligibly different, and we adopted the average values for a global solution which is plotted in Figure 2. The errors for this adopted solution were estimated as the absolute value of the difference between the results for the $H\alpha-$ and $H\alpha+$ sets.

The model fit is generally satisfactory although clear deviations are present in some emission bullets (see also Fig. 4 in Vermeulen et al. (1993a)). According to the model fit, the time of the greatest velocity separation in the precessional period occurred on HJD 2,451,458.12 \pm 0.23 which is in good agreement with the precessional ephemeris of Goranskii et al. (1998a) (HJD 2,450,000.0 +162^d.15*E*). We will therefore calculate precessional phase, Ψ , in the remainder of this paper according to the ephemeris, HJD 2,451,458.12 +162.15*E*, so that $\Psi = 0$ corresponds to greatest radial velocity separation (and greatest disk opening angle). Note that in earlier work by Margon (1984) and others the precessional cycle was measured from the first radial velocity cross-over point which occurs at $\Psi = 0.342$ in our ephemeris.

The semiamplitude of the nodding motion is $\Delta z \approx 0.009$ which is in reasonable agreement with the ratio found by other investigators (0.007, Katz et al. (1982); 0.010, Kopylov et al. (1987); 0.006, Goranskii et al. (1998a)). The time t_{or} in the Katz et al. (1982) model corresponds to a quadrature phase in the binary orbit ($\phi = 0.25$ or 0.75 where orbital phase ϕ is reckoned from the time of mid-eclipse). It is interesting to note that our fitted value of t_{or} occurs at $\phi = 0.83$ according to the light curve ephemeris of Goranskii et al. (1998a), HJD 2,450,023.62 +13.08211*E* (which we use below for orbital phase calculations) or 1.0 d later than expected. The time t_{or} is also 0.7 d later than the predicted time of maximum light associated with the nodding motions according to the nutational ephemeris of Goranskii et al. (1998a) (HJD 2,450,000.94 +6.2877*E*). These facts suggest that there is time lag in the tidal response between the outer and inner parts of the precessing disk (Goranskii et al. 1998a).

Table 2 also gives our measured equivalent width values for the $H\alpha$ bullets which are comparable in range to those found in previous results (Vermeulen et al. 1993a). Panferov et al. (1997) describe evidence for systematic variations in bullet strength with precessional phase which they interpret as an emission anisotropy (stronger in the leading direction of the jets). Unfortunately, we lack the photometry needed to transform from continuum based emission strength to absolute emission flux, so our results are not suitable to address this issue. However, we can investigate how the equivalent width ratio $W_\lambda(H\alpha-)/W_\lambda(H\alpha+)$ varies with precessional phase (Asadullaev & Cherepashchuk 1986; Kopylov et al. 1987; Vermeulen et al. 1993a; Panferov et al. 1997). We assume that the local continuum distribution varies as the Rayleigh-Jeans part of a hot blackbody spectrum, so that the physical emission flux ratio is approximately equal to $[W_\lambda(H\alpha-)/W_\lambda(H\alpha+)](\lambda+/\lambda-)^4$ where $\lambda-$ and $\lambda+$ are the

observed bullet wavelengths (Vermeulen et al. 1993a). Figure 3 illustrates this physical ratio versus precessional phase (see also Fig. 6 of Panferov et al. (1997)). The solid circles represent ratios derived from the average for each run of all measurements with $|W_\lambda| > 10 \text{ \AA}$. Because the jets have attained modestly relativistic speeds, radiation from the approaching jet should appear boosted compared to the receding jet, and the ratio is expected to vary with precession phase as $[(1 + z_+)/ (1 + z_-)]^4$ (*solid line*) if the bullets can be considered as discrete components (Urry & Padovani 1995). The observed increase in the ratio when the jets are closest to our line of sight (at $\Psi = 0$) was also found by Asadullaev & Cherepashchuk (1986) and Panferov et al. (1997), and appears to be close to the predicted amount of boosting. On the other hand, Panferov et al. (1997) argue that the bullets in SS 433 should be regarded as a stream of individual gas clouds, in which case the the exponent in the above relation is decreased by one power of the Doppler factor because of Lorentz contraction (Urry & Padovani 1995). If so, then relativistic boosting (*dotted line*) is insufficient to account for observed overluminosity of the approaching bullets, and the relative weakness of the receding bullets might be due to some increase in intervening opacity (perhaps from the disk) near $\Psi = 0$ (Panferov et al. 1997). Note that these expressions are based upon the assumption that the lines are broad enough that transformations appropriate for broad-band, rather than fixed frequency, emission are being considered.

4. Stationary Emission Lines

The most striking features in our optical spectra are the so-called “stationary lines” of $H\alpha$ and He I $\lambda\lambda 5876, 6678, 7065$ (Crampton & Hutchings 1981; Margon 1984; Falomo et al. 1987; Zwitter et al. 1989; Kopylov et al. 1989; Vermeulen et al. 1993a; Fabrika 1997). These lines do, in fact, display small radial velocity shifts that are related to orbital phase, but the interpretation of the variations is still a matter of debate (see below). Here we describe the overall appearance of these lines and their variations both between and within runs.

The average $H\alpha$ profiles for each run are plotted as a function of radial velocity and date in Figure 4. The profile is characterized by a central emission core and broad wings that extend to $\pm 2000 \text{ km s}^{-1}$. Both core and wings are time variable, and during one run (around HJD 2,451,426) the feature developed into a conspicuous P Cygni profile with a blue-shifted absorption trough. Other investigators (Crampton & Hutchings 1981; Kopylov et al. 1989; Fabrika 1997) have found similar P Cygni profiles usually during precessional phases when the jet axis is normal to our line of sight (and the disk is nearly edge-on) which occurs in the range $\Psi \approx 0.3 - 0.7$, but the P Cygni feature appears in our data after this interval. We also show in Figure 4 the mean profile from our 1998 run inserted at a date

corresponding to its precessional phase. There is no clear evidence in our set of spectra of strength or shape variations that are related to precessional phase.

The mean profiles of He I $\lambda\lambda 5876, 6678, 7065$ are illustrated in a similar format in Figure 5. They generally have a similar appearance to one another and to the H α core, and the P Cygni episode noted above in H α is also clearly evident in all three He I lines as well as O I $\lambda 7772$ (which sometimes has absorption as deep as 50% of the continuum). The P Cygni shape is also seen in two earlier runs in He I $\lambda 5876$ alone. The He I profiles sometimes show a double-peaked emission maximum which also occurs in H α . The broad emission wings seen in H α are generally not found in the He I profiles, except during the final run when the wings were very strong in H α . We also note the development during the last two runs of blue-shifted Na I $\lambda\lambda 5890, 5896$ emission which appeared at a radial velocity of -27 km s^{-1} (compared to the mean interstellar Na D absorption velocity of $+35 \text{ km s}^{-1}$).

The evolution of the H α profiles on shorter time scales is shown for two runs in Figures 6 and 7. Both plots indicate that the profile is constantly varying with somewhat more rapid (night-to-night) changes occurring in the broad wings. Two examples of the wing variations are particularly noteworthy. Figure 6 shows that the blue emission wing was very strong around HJD 2,451,357, and several, weak absorption troughs are visible. One of these troughs apparently migrated bluewards during this run at a nearly constant acceleration of $\approx -30 \text{ km s}^{-1} \text{ d}^{-1}$ (*dotted line*), reaching -539 km s^{-1} in the last spectrum of the run. Figure 7 shows another outwardly accelerating feature, this time seen in emission in the red wing of the profile (*dotted line*). This feature was seen to grow and decline over a period of 3 d with an acceleration of $\approx +92 \text{ km s}^{-1} \text{ d}^{-1}$, and it was last clearly visible at a radial velocity of $+1234 \text{ km s}^{-1}$. These kinds of outwardly moving sub-features are also observed in the emission lines of Wolf-Rayet stars (Lépine et al. 2000) where they are interpreted as evidence of clumping in the wind outflow.

We measured the equivalent width (W_λ), FWHM, and radial velocity for the stationary lines of H α and He I $\lambda\lambda 5876, 6678, 7065$, and the results are collected in Tables 4 and 5, respectively. The profiles are complex and asymmetric, and so we made two radial velocity measurements, an intensity weighted centroid of the entire profile (V_{centroid}) and a parabolic fit of the upper third of the emission peak (V_{peak}). Several of the He I lines posed special problems. We measured only the emission portion of those with P Cygni profiles, and we did not include the weak and broad emission component that appeared in the last run. The Na D lines acted as an arbitrary boundary for the integration of equivalent width for He I $\lambda 5876$. We then searched for correlated variations in the measurements with the orbital and precessional phases, and except in the case of V_{peak} (see below), we found no compelling evidence of variability related to either of these clocks. The lack of correlation is surprising

since other investigators have claimed orbital and precessional related velocity and strength variations in earlier observations (Zwitter et al. 1989; Kopylov et al. 1989; Fabrika 1997). There is no apparent change in H α emission equivalent width during the photometric primary eclipse, in agreement with the results of Goranskii et al. (1997). There is also no evidence of precessional related variations in H α FWHM, which would be expected if the emission formed in a disk which changes orientation with precession. For example, according to the kinematical model for the jets (Margon & Anderson 1989), we would expect the sine of the angle between the disk normal and observer to be about 0.86 at greatest disk opening (precessional phase $\Psi = 0$) compared to 1.00 at the disk edge-on orientation ($\Psi = 0.34$ and 0.66), and therefore, lines broadened by disk rotation would vary in width concurrently. However, even if such variations are present, they are overwhelmed by larger, temporal variations in width (for example, an increase by a factor of 2 over the duration of the final run).

The one correlation that did emerge is the variation in V_{peak} with orbital phase. We found that in each run this radial velocity attained a different maximum near orbital phase $\phi = 0$, the time of primary eclipse. In order to compare the results from different runs, we applied an offset to each set of radial velocities which was calculated to minimize the scatter around a common sinusoidal curve. The sinusoidal fit parameters are given in Table 6 where K represents the semiamplitude of variation, $\phi(\text{max.})$ is the orbital phase of maximum radial velocity, V_n is the systemic radial velocity found in run number n (see Table 1), and r.m.s. is the root mean square of the residuals from the fit. The differential velocity measurements and fits are illustrated in Figure 8. Our results agree reasonably well with earlier estimates ($K = 73 \pm 4 \text{ km s}^{-1}$, Crampton et al. (1980)), but there appears to be considerable cycle-to-cycle variations in semiamplitude which may explain differences found between investigators. As noted first by Crampton & Hutchings (1981), the occurrence of a velocity maximum at orbital conjunction implies that we are *not* measuring Keplerian motion in these features. Fabrika (1997) suggests that the systemic velocity of the stationary lines varies in step with precessional phase (see his Fig. 2), and our results confirm that the systemic velocities tend to be lower near $\Psi = 0$. This may reflect differing amounts of subtle, blue-shifted absorption is the wind outflow that has greatest effect when the disk has an edge-on orientation ($\Psi = 0.3 - 0.7$).

Fabrika (1997) and others have demonstrated that the high excitation He II $\lambda 4686$ line attains maximum radial velocity at orbital phase $\phi = 0.75$ which is consistent with the expected orbital motion of emitting gas near the X-ray source. We found only one example of such Doppler shifts in the spectral range we observed, in the weak emission line blend of C II $\lambda\lambda 7231, 7236$ (see Fig. 10 in the next section). This feature is seen in emission in stars with strong winds, such as cool W-R stars and luminous blue variables like P Cygni (Stahl

et al. 1993). The line is difficult to measure because it falls in a region of strong atmospheric lines and lies close to the weak Ne I $\lambda 7245$ emission line from city lights. Nevertheless, it appears double-peaked in our best spectra with the same separation as the C II features, which strengthens the case for its identification. We measured centroid velocities for this feature in those spectra where the emission was readily detected, and these radial velocities are plotted versus orbital phase in Figure 9 (for an assumed rest wavelength equal to the mean of the two, 7233.9 \AA). Unlike the H α and He I stationary line velocity curves, this line appears to reach maximum velocity at phase 0.75 (although the actual maximum velocity may vary from cycle to cycle). A sinusoidal fit with the maximum set at this value yields a semiamplitude, $K = 162 \pm 29 \text{ km s}^{-1}$ and a systemic velocity, $V_0 = 200 \pm 20 \text{ km s}^{-1}$, in reasonable agreement with the velocity curve of He II $\lambda 4686$ (Fabrika 1997). If we assume that the velocity curve represents orbital motion, then this feature, like He II $\lambda 4686$, probably forms close to the X-ray source in a region surrounding the disk center.

Our results for the strong H α and He I stationary lines are best explained if these lines originate in a wind outflow from the accretion disk (Goranskii et al. 1997) rather than in the disk itself or in a gas stream. The overall H α shape varies from a strong, rounded top emission line to a weaker, P Cygni profile which certainly implicates a mass outflow. Castor (1970) showed in some of the first models for winds from stars that optically thick outflows produce strong, rounded-top profiles with no blue absorption while P Cygni profiles are associated with more optically thin winds. Modern models for winds from the accretion disks in cataclysmic variables (Knigge et al. 1995; Feldmeier & Shlosman 1999; Feldmeier et al. 1999) show that winds from disks can also produce P Cygni and single peaked emission lines depending in part on disk orientation. The change between P Cygni and single peak appearance in our data does not appear to be strictly related to precessional phase (disk orientation), so the variations we observe in the stationary lines of SS 433 probably result at least partially from temporal changes in the wind structure instead of changes in orientation.

Indeed the observations point to a wind outflow that is constantly changing. We observe long term changes (weeks) in overall strength and radial velocity that probably correspond to global changes in the disk-wind outflow, plus we find rapid variations (days), such as the accelerating features in the H α wings, that suggest the development of clumping or other shock structures in the wind. The appearance of blue-shifted Na D emission in the last runs suggests the presence of outflowing structures forming at a large distance from the binary where the gas can cool.

The variation in V_{peak} with orbital phase (Fig. 8) is probably due to the influence of the mass donor star on the structure of the accretion disk’s wind (Goranskii et al. 1998a). The companion is probably a large and hot star (Goranskii et al. 1998a; King et al. 2000) with

significant radiative flux and possibly a wind of its own. This star could effectively remove the disk-wind outflow in its vicinity by direct blockage of the flow (Goranskii et al. 1998a), through the formation of a colliding winds bow shock between the stars (Cherepashchuk et al. 1995), or through photoionization (Hatchett & McCray 1977) (see the case of Cyg X-3; van Kerkwijk et al. (1996)). In the case of H α , the reduction in flux could be caused by heating of the gas in the vicinity of the donor star and a subsequent decrease in H α emissivity (Richards & Ratliff 1998). Thus, when we observe the system near primary eclipse, $\phi = 0$, a portion of disk-wind volume in the foreground surrounding the companion is absent, and there is a net decrease in blue-shifted emission (yielding a red-shift in the remaining emission envelope). Likewise, at $\phi = 0.5$, the evacuated region occurs in the region moving away from us, so that the red-shifted emission declines. The fact that this V_{peak} variation appears different from orbit to orbit suggests that there are temporal variations in the boundary or shape of the evacuated region. Note that the gas stream model for the H α stationary line (Crampton & Hutchings 1981; Kopylov et al. 1989) is not viable, since a Roche lobe overflow stream from the donor would be eclipsed near or shortly after $\phi = 0$ which we do not observe.

Disk-wind models for cataclysmic variables (Knigge et al. 1995; Feldmeier & Shlosman 1999; Feldmeier et al. 1999) show that the inner disk produces a faster flow, more collimated with the disk normal, while the outer portions produce a slower, dense wind that flows closer to the disk plane. We speculate that the wings and core of the stationary H α emission correspond to these two outflow regimes, respectively, since the wings have the large velocities and rapid variability expected in the inner disk, high speed wind. The outer disk wind may be the source of an extended circumbinary gas torus, and such a region was recently discovered by Paragi et al. (1999) in radio emitting clouds normal to the jet axis.

5. The Continuum Spectrum

The spectral features described thus far are probably formed in outflows from the system, and it is important to check for any features that might form in the donor star or disk. Such features would display modest Doppler shifts (probably $< 200 \text{ km s}^{-1}$), and so we formed a simple average spectrum to search for any weak features associated with the star or disk. We first subtracted out the Gaussian fits made of the moving H α features (Table 2), and then at each wavelength point we formed the mean and standard deviation, σ , from all our available spectra, and finally we formed a second mean after deletion of any points more than 2σ away from the first mean. We then made a careful inspection of the spectrum for interstellar absorption lines (mainly diffuse interstellar bands) from the lists of Herbig (1975), Herbig & Leka (1991), Morton (1991), and especially Galazutdinov et al. (2000),

and an interstellar spectrum was formed by extracting the mean SS 433 spectrum in the immediate vicinity of each interstellar absorption line. This spectrum of interstellar features appears in Figure 10, and it bears a strong resemblance to the mean interstellar spectrum of heavily reddened stars published by Jenniskens & Désert (1994) (see their Fig. 4). The mean SS 433 spectrum divided by the interstellar spectrum appears in Figure 10 along with a sample night sky absorption spectrum and the spectrum of a hot star, 9 Cep (B2 Ib) (with interstellar lines removed). All of these spectra were smoothed by convolution with a Gaussian filter of $\text{FWHM} = 100 \text{ km s}^{-1}$ (5 pixels).

The red spectral range of SS 433 is marked by the strong “stationary” features ($\text{H}\alpha$, He I $\lambda\lambda 5876, 6678, 7065$) plus the weaker features of C II $\lambda\lambda 7231, 7236$, He I $\lambda 7281$, and O I $\lambda 7772$. The remaining features may represent very weak stationary lines (see for comparison the wind outflow lines in the P Cygni spectral atlas by Stahl et al. (1993)), but they could also be due to residual flat fielding problems, problems in dividing out the night sky absorption (near 6868 and 7605 Å), air glow emission lines (many weak lines such as OH at 7712 Å), incomplete removal of broad interstellar features (such as the broad profile near 6172 Å; Galazutdinov et al. (2000)), and incomplete removal of weak jet features. There are no stellar absorption lines present deeper than 5% of the continuum with the exception of the P Cygni trough of O I $\lambda 7772$. The donor star is expected to contribute an increased fraction of the flux during primary eclipse, and so we also examined an eclipse spectrum made at HJD 2,451,357.8 but found no evidence of additional absorption lines.

The spectrum of 9 Cep (B2 Ib) illustrated in Figure 10 shows the kinds of spectral lines we might expect to find if the donor was a typical, early B-type star. The strong lines in such a spectrum are the same set that forms the stationary emission lines in SS 433, and since the emission from outflows dominates in these features, they cannot be used easily to find the donor’s spectrum. The only other features available in this region cluster near 5700 Å (including N II $\lambda\lambda 5666, 5679, 5710$, Al III $\lambda\lambda 5696, 5722$, and Si III $\lambda 5739$), but there are no corresponding absorption lines in the SS 433 spectrum. If the donor was an O-type star, we might expect to find transitions of He II $\lambda 5411$, O III $\lambda 5592$, C III $\lambda 5696$, and C IV $\lambda\lambda 5801, 5812$ (Conti 1974), but there is no evidence of these lines in the SS 433 spectrum either. A cooler donor might more easily escape detection in this spectral region, but even in the case of a cooler B-type star, we might expect to find transitions like Si II + Mg II $\lambda 6347$, Si II $\lambda 6371$, and Ne I $\lambda 6402$ (Galazutdinov et al. 2000). Again we find no trace of these absorption lines in the SS 433 spectrum.

We also used a Doppler tomography algorithm (Bagnuolo et al. 1994) to make trial reconstructions of the donor star spectrum for assumed values of semiamplitude, $K_O = 80 - 320 \text{ km s}^{-1}$ (Antokhina & Cherepashchuk 1987), $K_X = 175 \text{ km s}^{-1}$ (Fabrika 1997),

and flux ratio, $F_O/(F_O + F_X) = 0.25$. We restricted the sample to the KPNO spectra from 1999 to insure a homogeneous set of spectra, and the jet components were divided out prior to reconstruction. The algorithm assumes that the spectrum features can be assigned to a disk or donor component with radial velocity variations defined by the photometric phase of observation and assumed semi-amplitudes, and so the strong stationary lines, which follow neither curve, are arbitrarily divided between the disk and star components in the reconstruction. We searched for stellar lines away from these emission artifacts, but again there were no stellar absorptions visible with depths exceeding 10% of the continuum. Since O- and B-type stars generally have metallic line depths of this order in this red region (for moderate projected rotational velocities), our null detection of such absorption lines implies that a normal companion can contribute no more than 25% of the continuum flux in this part of the spectrum, in agreement with estimates from analyses of the optical light curve (Leibowitz 1984; Antokhina & Cherepashchuk 1987; Sanbuichi & Fukue 1993). However, we suspect that the photosphere of the donor star remains hidden behind the veil of the disk wind, and so such limits on the donor’s flux contribution based on line depths should be treated with caution.

6. UV Spectrum

Our original goal in this program was to obtain *Hubble Space Telescope (HST)* Space Telescope Imaging Spectrograph (STIS) observations of the far ultraviolet spectrum at several points throughout the precessional period. However, our single observation (made on 1999 July 3) showed no easily detectable UV flux, and so subsequent planned observations were abandoned. Here we discuss this one null result and its implications for the UV spectral flux distribution.

The STIS observation was made with the first order G140L grating which covers the range 1150 – 1700 Å with a spectral resolution of $\lambda/\Delta\lambda = 1000$ (average reciprocal dispersion of 0.6 Å pixel⁻¹). The star was centered in the large 52 × 2 arcsec aperture, and the spectrum was recorded on the FUV-MAMA detector in ACCUM (integration) mode. The spectrum was made in three sub-exposures for a total of 7534 s of targeted exposure. The spectra were reduced with the standard STIS pipeline software using contemporary background, flux, and wavelength calibrations (Voit et al. 1997). The final product we examined was a co-added and flux calibrated image in rectified spatial and wavelength coordinates.

The image of the UV spectrum is dominated by broad bands of geocoronal emission (primarily near Ly α λ 1216 and O I $\lambda\lambda$ 1302, 1356) that span the full spatial dimension, and these are superimposed upon a very low level, diffuse background (Brown et al. 2000). A

visual inspection of the wavelength-summed spectrum along the spatial dimension showed no evidence of an obvious peak near the expected position of the stellar spectrum, nor any sign of an emission peak near $\text{Ly}\alpha$. Nevertheless, we attempted to extract the spectrum by first fitting a second order polynomial to the background at each wavelength point over the spatial pixel range $(-100 : -20, +20 : +100)$ relative to the predicted stellar spectrum position, and then this fit was subtracted and the net flux was integrated over 11 spatial pixels centered on the position of the stellar spectrum. The spatially integrated flux was then converted to units of $\text{erg cm}^{-2} \text{s}^{-1} \text{\AA}^{-1}$ using the averaged, point source, aperture throughput conversion factor (Voit et al. 1997). We then formed the average flux in wavelength bins of width approximately 50\AA that were selected to include regions of comparable background noise (for example, by selecting bin boundaries that coincide with the ranges of the geocoronal emission features), and we also calculated the standard deviation of the mean, σ_μ , in each of these samples (Table 7). In no case did we find a mean that exceeded $3\sigma_\mu$, and so we cannot claim that the UV flux of SS 433 was actually detected. Instead, we set upper limits for any such flux as the sum of the mean flux plus twice the standard deviation of the mean. Even if the stellar spectrum was misplaced from the expected spatial position, the upper limits should reflect the noise character found in nearby parts of the image. These upper limits are plotted in Figure 11.

The only reliable detection of SS 433 in the UV band was made with the *HST* High Speed Photometer (HSP) by Dolan et al. (1997), and it is worthwhile comparing our far-UV limits with their near-UV measurements. Dolan et al. (1997) observed SS 433 at epochs when the system is generally brighter and fainter in the precessional cycle (corresponding to times when the disk face is maximally opened in our direction and edge-on, respectively), and we show in Figure 11 the average flux they detected for both states in a filter centered on 2770\AA . There exists only one low dispersion spectrum of SS 433 in this spectral region in the archive of the *International Ultraviolet Explorer Satellite (IUE)* (LWR4698, obtained by Dr. A. Underhill), and we also show in Figure 11 the mean flux measured in three bins of 50\AA width in the best exposed part of that spectrum. The optical spectrophotometry from Wagner (1986) is illustrated for average bright ($0.8 < \Psi < 0.2$) and faint ($0.2 < \Psi < 0.8$) states.

Dolan et al. (1997) fitted the bright state near-UV and optical fluxes with a reddened blackbody spectral distribution for $T = 72,000 \text{ K}$ and $A_V = 8.4$, and we have used these parameters to calculate the predicted far-UV fluxes using the interstellar extinction curve defined by Fitzpatrick (1999) (for an assumed $R = A_V/E(B - V) = 3.1$). The extrapolation of the Dolan et al. (1997) flux distribution into the far-UV (*dotted line*) predicts fluxes that we would have detected around 1500\AA . Furthermore, the 2770\AA and red fluxes for the high state do not match the curve particularly well. Wagner (1986) finds a better

match with a lower extinction, $A_V = 7.8 \pm 0.5$, which agrees with estimates from other investigators (Murdin et al. 1980; Cherepashchuk et al. 1982). His fit of the high state optical fluxes indicates a blackbody temperature of $T = 45,000$ K, and this curve (*dashed line*) also predicts UV fluxes that we would have detected. However, the STIS spectrum was obtained on HJD 2,451,362.99 which corresponds to precessional phase $\Psi = 0.41$, close to the disk edge-on configuration when the system is fainter. In fact, a comparison of the counts in the STIS acquisition image with those predicted from the STIS Exposure Time Calculator ⁷ indicates that at the time of our observation SS 433 was only 1.2 times brighter than the average faint state spectrum of Wagner (1986). Thus, a better comparison might be made with the faint state fit given by Wagner (1986) (for $T = 21,000$ K and $A_V = 7.8$). This fit (*solid line*) predicts fluxes which fall just below our STIS detection limits. A low temperature like this is more consistent with the UV flux observed in another X-ray binary, LMC X-3 (fit with $T = 30,000$ K), in which the disk out shines the stellar flux contributions (Cowley et al. 1994). Note that the spectral flux distribution of a super-Eddington accretion disk may depart from blackbody expectations especially at shorter wavelengths (Lipunov 1999; Okuda & Fujita 2000).

7. Discussion

Our objective in this final section is to relate the various spectral components discussed above to specific parts of the binary system. The well established components of SS 433 include the mass donor star (which must be close to Roche-filling in order to transfer mass to the the disk and power the X-ray source), the relativistic star (neutron star or black hole), the super-Eddington accretion disk and its wind, and the jets. The binary period is well known from the optical light curve (Goranskii et al. 1998a), and the system inclination is determined from the kinematical model for the jets (Margon & Anderson 1989). However, there still exists considerable uncertainty about the binary orbital velocity curves (and thus the size of the semimajor axis) and mass ratio. The radial velocity curve of the disk is measured indirectly through the Doppler shifts in the He II $\lambda 4686$ emission line which is probably formed in a hot gas outflow near the base of the jets (Goranskii et al. 1997; Fabrika 1997). The shape of the He II $\lambda 4686$ velocity curve changes with precessional phase (Fabrika et al. 1997), and Fabrika (1997) argues that the curve obtained near maximum disk opening angle ($\Psi = 0$) offers the best estimate of the disk’s orbital motion. The observed semiamplitude, $K \approx 175$ km s⁻¹, yields a mass function for the system inclination ($i = 79^\circ$) of approximately $M_O^3/(M_O + M_X)^2 = M_O/(1 + q)^2 = 7.7M_\odot$, where $q = M_X/M_O$. The semimajor axis is then

⁷http://garnet.stsci.edu/STIS/ETC/stis_acq_etc.html

given by $a = (1 + q)a_X = (1 + q) 3.2 \times 10^{12}$ cm (or $(1 + q)46R_\odot$). Analysis of the optical light curve yields mass ratio estimates from $q = 0.4$ to 1.2 (Antokhina & Cherepashchuk 1987; Fukue et al. 1998) while models of the X-ray light curve suggest a lower range, $q = 0.15$ to 0.25 (Antokhina et al. 1992).

The optical light curve (Goranskii et al. 1998a) provides some guidance about the proportions of the continuum flux that originate in the disk and star. The mean, out of eclipse, V-band magnitude exhibits a 0.60 mag variation through the precessional cycle (that tracks with the motion of the jets) which indicates that changes in disk orientation cause a modulation of 55% of the total flux. A variation this large is only possible if the disk is the dominant source of light in the optical. Furthermore, even during the center of the primary eclipse, the precessional light curve varies by 0.41 mag (Goranskii et al. 1998a) which suggests that the disk contributes a considerable fraction of the flux even during these partial eclipses. We can estimate the size of the continuum forming region using the blackbody fits to the flux distribution given in §6. The continuous spectrum fits shown in Figure 11 are normalized for a projected disk radius of 1.4×10^{12} cm ($20 R_\odot$) and of 2.3×10^{12} cm ($33 R_\odot$) for the high and low states, respectively, based on the temperature fits of Wagner (1986) and an assumed distance of 4.85 kpc (Vermeulen et al. 1993b). When the disk face attains its maximal opening towards us in the high state, we may be seeing the hotter, central regions of the disk, while during the edge-on, low state, we view more flux contributions from the outer (larger) regions of the disk. The low state radius is approximately half the semimajor axis for reasonable values of the mass ratio, and so we should admit the possibility that the continuum forming part of the disk may extend beyond the Roche lobe of the relativistic object.

Next we turn to the formation sites of the emission lines. The moving emission lines form in the relativistic jets (§3), and based upon their average lifetime and outflow velocity, these probably form at a distance of $\approx 4 \times 10^{14}$ cm ($6000R_\odot$) from the central engine, i.e., $\approx 100\times$ further out than the binary separation (Panferov 1999). On the other hand, we argued above (§4) that the stationary emission lines form in the disk wind with dimensions more comparable to the system separation. Murdin et al. (1980) show that the remarkable strength of the $H\alpha$ emission peak relative to the surrounding continuum implies that the $H\alpha$ emission is formed over a radius at least $10\times$ larger than the continuum source, which implies that line emitting regions of the disk wind extend far beyond the binary system. The optical star must be orbiting within a dense part of this outflow, and it apparently sculpts out a wind evacuated region in its immediate vicinity (through physical blockage, ionization of the nearby gas, or colliding winds) that leads to the orbital radial velocity variation we observe (Fig. 8).

Evidence of the interaction between the disk wind and star is probably also found in the X-ray light curve. We constructed a contemporary X-ray light curve using raw counts of the source from the Rossi X-ray Timer Explorer Satellite’s All Sky Monitor (RXTE/ASM) instrument⁸ (Levine et al. 1996). The ASM is sensitive to X-rays in the 1.5 – 12 keV range, and some 1673 measurements are available of SS 433 over the time interval JD 2,450,089 – 2,452,054. We selectively deleted those observations of high flux made during flaring events and those with net negative fluxes (null detections perhaps associated with X-ray dimming events comparable to those observed in the optical; Goranskii et al. (1998a)) to arrive at 1363 observations that correspond to the quiescent X-ray state. Figure 12 (*top panel*) illustrates the X-ray fluxes binned into 10 intervals of precessional phase (based on our precessional ephemeris). The X-ray flux clearly reaches a maximum near $\Psi = 0$, the phase of maximum disk opening, as has been found in earlier work (Yuan et al. 1995). If we restrict the ASM measurements to $\Psi = 0.8 - 0.2$, the phase interval surrounding the maximum, we also see evidence of X-ray flux variations nearly in step with the optical variations on the nutational periodicity, 6.2877 d (Goranskii et al. 1998a), caused by the nodding motions of the disk (Fig. 12, *lower panel*). The X-ray variations on the orbital cycle are shown in the central panels of Figure 12 for the disk opening ($\Psi = 0.8 - 0.2$) and disk edge-on ($\Psi = 0.2 - 0.8$) configurations during the precessional cycle. A significant X-ray eclipse is only observed in the disk opening state (*second panel from the top*), and the primary eclipse appears to be delayed or extended beyond the expected time around optical star inferior conjunction ($\phi = 0$), referred to as a “second eclipse” by Yuan et al. (1995). We suggest that this extended eclipse is caused by dense, X-ray opaque gas that trails behind the optical star as it plows through the disk wind. Earlier interpretations of the X-ray light curve required a large optical star (and therefore small mass ratio, q) in order to explain the long duration of the eclipses (Antokhina et al. 1992), and it would be rewarding to revisit the fits of the light curve taking full account of a wake induced extension of the eclipse. We note that a minor additional X-ray eclipse occurs at $\phi = 0.5$ when the disk is in the foreground. This suggests that an additional source of X-rays exists between the stars, and we tentatively suggest that a small fraction of the X-ray flux forms in a colliding winds shock near the optical star (Cherepashchuk et al. 1995).

All these observations suggest that the central binary is embedded in a large equatorial disk that is formed by the disk wind and extends far beyond the binary itself. Large outflowing disks are found in other massive binary systems, in particular, the W Serpentis class (Tarasov 2000) which includes such noteworthy examples as β Lyr (Linnell 2000) and RY Scuti (Smith et al. 1999). In the case of β Lyr, the disk is so thick that it blocks the

⁸<http://xte.mit.edu/>

photospheric flux of the mass gainer. The outer portions of the disk in SS 433 have recently been detected in the radio continuum by Paragi et al. (1999) at a projected separation of ≈ 50 mas or 4×10^{15} cm ($50,000 R_{\odot}$) away from the central binary. Variations in the inner portion of the disk may be responsible for the irregular changes in the red flux component discussed by Goranskii et al. (1998b).

The disk probably widens significantly with distance from the binary due to the changing orientation of the disk wind source with precession, and we suggest that the disk blocks our view to the central binary at almost all precessional phases except perhaps near $\Psi = 0$. The high opacity of the disk in the edge-on configuration reduces the X-ray and optical eclipse visibility during that part of the precessional cycle. Therefore, the best opportunity to observe directly the companion star is probably near $\Psi = 0$ when the disk obscuration attains a minimum (and not during the edge-on phases as suggested in the past; c.f. Leibowitz (1984)) and when the optical star is well in the foreground (near $\phi = 0$). We have a few spectra that satisfy these stringent timing requirements (obtained over 3 nights beginning on HJD 2,451,463), and it is interesting to note that a central absorption feature was visible in the He I features at that time that migrated redward as expected for the orbital motion of the optical star (see Fig. 13). The radial velocity shift is consistent with $K_O = 126 \pm 26$ km s $^{-1}$, which, when combined with $K_X = 175 \pm 20$ km s $^{-1}$ and $i = 79$, yields $q = 0.72 \pm 0.17$, $M_X/M_{\odot} = 16 \pm 6$, and $M_O/M_{\odot} = 23 \pm 8$. However, other interpretations of this feature are possible, and additional radial velocities derived from photospheric absorption lines are needed to obtain reliable mass estimates. High resolution spectroscopy in the blue (where metallic absorption features are more common in B-type spectra) during times of favorable orientation might well yield a reliable detection of the optical companion.

We thank the KPNO staff, and in particular Diane Harmer and Daryl Willmarth, for their assistance in making these observations with the KPNO Coude Feed Telescope, and we also thank Tammy Josephs for observing assistance at KPNO. We are grateful to the staff of McDonald Observatory and Tom Montemayor for their help at the 2.1-m telescope. This research has made use of results provided by the ASM/RXTE teams at MIT and at the RXTE SOF and GOF at the NASA/Goddard Space Flight Center. Support for this work was provided by NASA through grant number GO-8308 from the Space Telescope Science Institute, which is operated by the Association of Universities for Research in Astronomy, Inc., under NASA contract NAS5-26555. Institutional support has been provided from the GSU College of Arts and Sciences and from the Research Program Enhancement fund of the Board of Regents of the University System of Georgia, administered through the GSU Office of the Vice President for Research and Sponsored Programs. We gratefully acknowledge all this support.

REFERENCES

- Abell, G. O., & Margon, B. 1979, *Nature*, 279, 701
- Antokhina, E. A., & Cherepashchuk, A. M. 1987, *Soviet Astr.*, 31, 295
- Antokhina, E. A., Seifina, E. V., & Cherepashchuk, A. M. 1992, *Soviet Astr.*, 36, 143
- Asadullaev, S. S., & Cherepashchuk, A. M. 1986, *Soviet Astr.*, 30, 57
- Bagnuolo, W. G., Jr., Gies, D. R., Hahula, M. E., Wiemker, R., & Wiggs, M. S. 1994, *ApJ*, 423, 446
- Borisov, N. V., & Fabrika, S. N. 1987, *Soviet Astr. Lett.*, 13, 200
- Brown, T. M., Kimble, R. A., Ferguson, H. C., Gardner, J. P., Collins, N. R., & Hill, R. S. 2000, *AJ*, 120, 1153
- Castor, J. 1970, *MNRAS*, 149, 111
- Cherepashchuk, A. M., Aslanov, A. A., & Kornilov, V. G. 1982, *Soviet Astr.*, 26, 697
- Cherepashchuk, A. M., Bychkov, K. V., & Seifina, E. V. 1995, *Ap&SS*, 229, 33
- Clark, D. H. 1985, *The Quest for SS433* (New York: Viking Penguin)
- Collins, G. W., II, & Garasi, C. J. 1994, *ApJ*, 431, 836
- Conti, P. S. 1974, *ApJ*, 187, 539
- Crampton, D., Cowley, A. P., & Hutchings, J. B. 1980, *ApJ*, 235, L131
- Crampton, D., & Hutchings, J. B. 1981, *ApJ*, 251, 604
- Cowley, A. P., Schmidtke, P. C., Hutchings, J. B., & Crampton, D. 1994, *ApJ*, 429, 826
- D’Odorico, S., Oosterloo, T., Zwitter, T., & Calvani, M. 1991, *Nature*, 353, 329
- Dolan, J. F., et al. 1997, *A&A*, 327, 648
- Fabian, A. C., & Rees, M. J. 1979, *MNRAS*, 187, 13P
- Fabrika, S. N. 1997, *Ap&SS*, 252, 439
- Fabrika, S. N., Bychkova, L. V., & Panferov, A. A. 1997, *Bull. Special Astrophys. Obs.*, 43, 75

- Falomo, R., Boksenberg, A., Tanzi, E. G., Tarengi, M., & Treves, A. 1987, MNRAS, 224, 323
- Feldmeier, A., & Shlosman, I. 1999, ApJ, 526, 344
- Feldmeier, A., Shlosman, I., & Vitello, P. 1999, ApJ, 526, 357
- Fitzpatrick, E. L. 1999, PASP, 111, 63
- Fukue, J., Obana, Y., & Okugami, M. 1998, PASJ, 50, 81
- Galazutdinov, G. A., Musaev, F. A., Krelowski, J., & Walker, G. A. H. 2000, PASP, 112, 648
- Goranskii, V. P., Fabrika, S. N., Rakhimov, V. Yu., Panferov, A. A., Belov, A. N., & Bychkova, L. V. 1997, Astr. Rep., 41, 656
- Goranskii, V. P., Esipov, V. F., & Cherepashchuk, A. M. 1998a, Astr. Rep., 42, 209
- Goranskii, V. P., Esipov, V. F., & Cherepashchuk, A. M. 1998b, Astr. Rep., 42, 336
- Hatchett, S., & McCray, R. 1977, ApJ, 211, 552
- Herbig, G. H. 1975, ApJ, 196, 129
- Herbig, G. H., & Leka, K. D. 1991, ApJ, 382, 193
- Inoue, H., Shibazaki, N., & Hoshi, R. 2001, PASJ, 53, 127
- Jenniskens, P., & Désert, F.-X. 1994, A&AS, 106, 39
- Katz, J. I., Anderson, S. F., Margon, B., & Grandi, S. A. 1982, ApJ, 260, 780
- King, A. R., Taam, R. E., & Begelman, M. C. 2000, ApJ, 530, L25
- Knigge, C., Woods, J. A., & Drew, E. 1995, MNRAS, 273, 225
- Kopylov, I. M., Bychkova, L. V., Fabrika, S. N., Kumaigorodskaya, R. N., & Somova, T. A. 1989, Soviet Astron. Lett., 15, 474
- Kopylov, I. M., Kumaigorodskaya, R. N., Somov, N. N., Somova, T. A., & Fabrika, S. N. 1986, Soviet Astron., 30, 408
- Kopylov, I. M., Kumaigorodskaya, R. N., Somov, N. N., Somova, T. A., & Fabrika, S. N. 1987, Soviet Astron., 31, 410

- Leibowitz, E. M. 1984, MNRAS, 210, 279
- Lépine, S., et al. 2000, AJ, 120, 3201
- Levine, A. M., et al. 1996, ApJ, 469, L33
- Linnell, A. P. 2000, MNRAS, 319, 255
- Lipunov, G. V. 1999, Astr. Lett., 25, 508
- Margon, B. 1984, ARA&A, 22, 507
- Margon, B., & Anderson, S. F. 1989, ApJ, 347, 448
- McCarthy, J. K., Sandiford, B. A., Boyd, D., & Booth, J. 1993, PASP, 105, 881
- Milgrom, M. 1979a, A&A, 73, L3
- Milgrom, M. 1979b, A&A, 78, L9
- Milgrom, M., Anderson, S. F., & Margon, B. 1982, ApJ, 256, 222
- Morton, D. C. 1991, ApJS, 77, 119
- Murdin, P., Clark, D. H., & Martin, P. G. 1980, MNRAS, 193, 135
- Ogilvie, G. I., & Dubus, G. 2001, MNRAS, 320, 485
- Okuda, T., & Fujita, M. 2000, PASJ, 52, L5
- Panferov, A. A. 1999, A&A, 351, 156
- Panferov, A. A., Fabrika, S. N., & Rakhimov, V. Yu. 1997, Astr. Rep, 41, 342
- Paragi, Z., Vermeulen, R. C., Fejes, I., Schilizzi, R. T., Spencer, R. E., & Stirling, A. M. 1999, A&A, 348, 910
- Richards, M. T., & Ratliff, M. A. 1998, ApJ, 493, 326
- Sanbuichi, K., & Fukue, J. 1993, PASJ, 45, 727
- Smith, N., Gehrz, R. D., Humphreys, R. M., Davidson, K., Jones, T. J., & Krautter, J. 1999, AJ, 118, 960
- Stahl, O., Mandel, H., Wolf, B., Gaeng, Th., Kaufer, A., Kneer, R., Szeifert, Th., & Zhao, F. 1993, A&AS, 99, 167

- Stewart, G. C., et al. 1987, MNRAS, 228, 293
- Tarasov, A. E. 2000, in *The Be Phenomenon in Early-type Stars*, IAU Colloquium 175, A.S.P. Conf. Series 214, ed. M. A. Smith, H. F. Henrichs, & J. Fabregat (San Francisco: A.S.P.), 644
- Urry, C. M., & Padovani, P. 1995, PASP, 107, 803
- van den Heuvel, E. P. J. 1981, *Vistas in Astr.*, 25, 95
- van Kerkwijk, M. H., Geballe, T. R., King, D. L., van der Klis, M., & van Paradijs, J. 1996, A&A, 314, 521
- Vermeulen, R. C., Schilizzi, R. T., Spencer, R. E., Romney, J. D., & Fejes, I. 1993b, A&A, 270, 177
- Vermeulen, R. C., et al. 1993a, A&A, 270, 204
- Voit, M., et al., ed. 1997, *HST Data Handbook* (Baltimore: Space Telescope Science Institute)
- Wagner, R. M. 1986, ApJ, 308, 152
- Wijers, R. A. M. J., & Pringle, J. E. 1999, MNRAS, 308, 207
- Yuan, W., Kawai, N., Brinkmann, W., & Matsuoka, M. 1995, A&A, 297, 451
- Zwitter, T., Calvani, M., Bodo, G., & Massaglia, S. 1989, *Fund. Cosmic Phys.*, 13, 309

Fig. 1.— The H α emission components from the jets over the last 7 nights of observation. The left panel shows the approaching jet components and the right panel shows the receding components (with a reversed wavelength scale so that the Doppler shifts can be easily compared between panels). Each spectrum is placed so that the continuum is aligned with the time of observation and is scaled in intensity so that the continuum strength is equivalent to 0.5 d on the y -axis. Tick marks indicate the central position of each component as determined by Gaussian fitting.

Fig. 2.— The radial velocity curves of the H α - (*filled circles*) and H α + (*open circles*) emission components (symbols are plotted with areas proportional to W_λ). The global fit made using the Katz et al. (1982) nodding motions model is shown as a solid line.

Fig. 3.— The ratio of the mean emission equivalent width for the approaching jet to that of the receding jet for each of the observing runs plotted as a function of jet precessional phase. The continuous lines show the predicted amount of relativistic boosting for Doppler exponents 4 (*solid*) and 3 (*dotted*).

Fig. 4.— Average H α stationary profiles plotted as a function of heliocentric radial velocity and date of run. The spectra are placed so that their continua are aligned with the mean date of observation, and the intensity scale in continuum units is given in the upper right corner. Each profile is labelled with the mean precessional phase. The dashed line gives the profile from the 1998 run placed at the time corresponding to its precessional phase in an earlier cycle. The left hand panel illustrates the development of Na I $\lambda\lambda 5890, 5896$ emission during the final two runs.

Fig. 5.— Average He I stationary profiles in the same format as Fig. 4. The dashed line in the middle panel for He I $\lambda 6678$ corresponds to the mean profile from the 1998 run plotted at a date corresponding to its precessional phase.

Fig. 6.— Individual H α stationary profiles from our longest run plotted as a function of heliocentric wavelength and time of observation (in the same way as Fig. 4). The corresponding orbital phase is indicated on the right hand side. The dashed line shows the fitted radial velocity curve for the H α + jet components (one of which appears near 6484\AA at HJD 2,451,364; other, weaker jet components may be blended with the stationary H α line in the preceding two nights). The nearly vertical dotted line traces the outward motion of a blue-shifted absorption trough.

Fig. 7.— Individual $H\alpha$ stationary profiles from our final run plotted in the same format as Fig. 6. Here the dashed line shows the fitted radial velocity curve for the $H\alpha$ – jet, while the dashed - triple dotted line shows the same for jet features of He I $\lambda 6678$. The dashed - single dotted line shows the radial velocity curve of the opposite red jet for He I $\lambda 5876$. No He I jet components are readily visible at their expected positions. The nearly vertical dotted line traces the outward motion of a red-shifted emission bump.

Fig. 8.— Radial velocity curves of the stationary line emission peaks. The measured relative velocities are shown for each observing run using the following symbols: 1 – X, 2 – plus sign, 3 – asterisk, 4 – diamond, 5 – triangle, and 6 – square. The solid lines show the sinusoidal fits for each (Table 6).

Fig. 9.— Radial velocity curve of the C II $\lambda\lambda 7231, 7236$ stationary emission line. Measurements from different runs are plotted using the same symbols as in Fig. 8. The solid line shows a sinusoidal fit to the entire set.

Fig. 10.— The average spectrum of SS 433 (*top*) after removal of the $H\alpha$ jet components and division of the interstellar spectrum (*third from top*, offset in intensity by -0.5 for clarity). Also shown are the absorption spectrum from Earth’s atmosphere (*bottom*, reduced by a factor of 2 in intensity and offset by -1.0) and the spectrum of 9 Cep (B2 Ib) (*second from top*, offset in intensity by -0.2 for clarity).

Fig. 11.— The observed and predicted spectral flux distribution of SS 433 in the ultraviolet and optical. The arrows at the shorter wavelengths illustrate the flux upper limits from the STIS observation. The line at the top of each arrow corresponds to the mean $+2\sigma_\mu$ flux limit over the wavelength range covered by the line. The tip of the lower part of the arrow gives the measured mean flux in the band (generally too small for reliable detection). The two error bars at 2770 \AA give the average bright and faint fluxes found by Dolan et al. (1997) using *HST*/HSP. The three error bars between 2900 \AA and 3000 \AA show the mean fluxes in *IUE* spectrum, LWR4698. The optical spectrophotometry from Wagner (1986) is averaged for the bright (*diamonds*) and faint (*squares*) states. Model fluxes for reddened blackbody curves are shown for $T = 72,000, 45,000, 21,000 \text{ K}$ and $A_V = 8.4, 7.8, 7.8$ (*dotted, dashed, solid lines*), respectively.

Fig. 12.— The RXTE/ASM X-ray count rates plotted against several of the SS 433 “clocks”. *Top*: Binned averages as a function of precessional phase where $\Psi = 0$ corresponds to maximum disk opening (epoch of greatest velocity separation in the jet components). *Second from top*: Data from near maximum disk opening plotted against orbital phase ($\phi = 0$ is the epoch of the primary optical eclipse). *Third from top*: Data from the more edge-on precessional phases plotted against orbital phase. *Bottom*: Data from near maximum disk opening plotted against nutational phase (0 corresponds to maximum optical light in the nodding cycle; Goranskii et al. (1998a)). Error bars show the standard deviation of the mean in each case.

Fig. 13.— He I $\lambda 6678$ profiles obtained near $\Psi = 0$ and $\phi = 0$ plotted in a format similar to Fig. 6. The tick marks indicate the positions of a central absorption feature that moved redward in this sequence in the manner expected for the optical star. The absorption feature disappeared on the subsequent 3 nights when the optical star was behind the disk.

Table 1. Journal of Optical Spectroscopy

Run Number	Dates (HJD-2,451,000)	Range (Å)	Resolution ($\lambda/\Delta\lambda$)	Number	Observatory/Telescope/ Grating/CCD
1	53.7 – 62.7	6313 – 6978	9530	5	KPNO/0.9m/B/F3KB
2	354.7 – 354.9	6431 – 6785	5440	2	KPNO/0.9m/RC181/TI5
2	355.7 – 364.9	5405 – 6743	3950	9	KPNO/0.9m/RC181/F3KB
2	355.9 – 365.0	6461 – 7799	4940	9	KPNO/0.9m/RC181/F3KB
3	395.9 – 399.9	5510 – 6854	41960	3	McD/2.1m/Echelle/RA2
4	421.7 – 429.7	5397 – 6735	4050	7	KPNO/0.9m/RC181/F3KB
4	421.7 – 429.6	6453 – 7791	4240	6	KPNO/0.9m/RC181/F3KB
5	463.7 – 467.7	5400 – 6736	4100	5	KPNO/0.9m/RC181/F3KB
5	463.6 – 468.7	6446 – 7782	5020	6	KPNO/0.9m/RC181/F3KB
6	491.6 – 497.6	5545 – 6881	4400	7	KPNO/0.9m/RC181/F3KB
6	491.6 – 497.6	6590 – 7927	5220	6	KPNO/0.9m/RC181/F3KB

Table 2. Jet Component Measurements

Date (HJD-2,451,000)	z ($\Delta\lambda/\lambda$)	W_λ (\AA)	FWHM (\AA)
H α – Components			
56.709	0.0503	-49	42
57.732	0.0519	-44	43
62.709	0.0634	-47	70
355.878	0.0499	-14	23
355.878	0.0560	-23	40
356.932	0.0588	-62	31
357.887	0.0602	-87	35
359.865	0.0538	-70	39
359.865	0.0587	-16	19
359.865	0.0626	-12	27
360.889	0.0526	-56	32
360.889	0.0580	-18	47
361.932	0.0530	-28	38
361.932	0.0640	-53	52
362.957	0.0529	-11	42
362.957	0.0656	-16	25
362.957	0.0720	-26	26
363.891	0.0649	-7	19
363.891	0.0718	-6	23
363.891	0.0787	-76	31
364.953	0.0599	-17	26
364.953	0.0655	-38	53
364.953	0.0781	-46	43
421.726	-0.0297	-19	61
424.717	-0.0303	-50	44
429.675	-0.0607	-24	36
463.674	-0.0901	-67	31
464.669	-0.0975	-19	30

Table 2—Continued

Date (HJD-2,451,000)	z ($\Delta\lambda/\lambda$)	W_λ (\AA)	FWHM (\AA)
464.669	-0.0935	-26	26
464.669	-0.0896	-11	22
465.674	-0.1039	-37	29
465.674	-0.0978	-12	17
465.674	-0.0923	-20	57
466.660	-0.1055	-42	35
466.660	-0.0974	-4	16
466.660	-0.0925	-10	53
467.672	-0.1058	-31	33
467.672	-0.0964	-35	74
491.644	-0.0500	-43	40
492.622	-0.0497	-13	42
492.622	-0.0333	-13	24
492.622	-0.0259	-19	30
493.612	-0.0218	-40	26
494.620	-0.0225	-83	31
495.623	-0.0249	-77	32
496.619	-0.0258	-60	26
497.623	-0.0266	-57	29
H α + Components			
53.674	-0.0095	-50	63
55.705	-0.0118	-51	45
56.709	-0.0124	-6	40
62.709	0.0148	-5	28
354.740	0.0266	-45	32
354.925	0.0259	-73	41
354.740	0.0182	-40	21
355.878	0.0181	-48	21

Table 2—Continued

Date (HJD-2,451,000)	z ($\Delta\lambda/\lambda$)	W_λ (\AA)	FWHM (\AA)
355.878	0.0266	-18	36
356.813	0.0121	-14	17
356.932	0.0118	-17	17
357.769	0.0116	-29	24
357.887	0.0119	-35	25
359.747	0.0192	-12	29
359.865	0.0268	-53	42
359.865	0.0193	-40	29
360.697	0.0155	-48	43
360.889	0.0271	-10	33
360.889	0.0171	-13	28
360.889	0.0131	-8	22
361.895	0.0135	-2	28
361.932	0.0132	-1	11
363.716	-0.0124	-50	25
363.891	-0.0120	-40	22
364.921	-0.0115	-14	27
364.953	-0.0115	-8	22
399.890	0.0112	-36	24
421.670	0.1274	-7	38
421.670	0.0901	-5	28
421.670	0.0841	-5	29
424.642	0.1078	-41	42
429.624	0.1423	-15	50
463.619	0.1533	-57	50
464.618	0.1600	-30	41
464.618	0.1529	-14	32
465.617	0.1686	-26	75
465.617	0.1601	-14	43
465.617	0.1525	-6	28

Table 2—Continued

Date (HJD-2,451,000)	z ($\Delta\lambda/\lambda$)	W_λ (\AA)	FWHM (\AA)
466.611	0.1737	-21	55
466.611	0.1602	-10	49
466.611	0.1518	-3	29
467.612	0.1738	-26	65
467.612	0.1641	-19	91
468.687	0.1731	-10	54
468.687	0.1585	-7	32
468.687	0.1521	-33	38
491.599	0.1257	-26	33
492.571	0.1251	-8	27
492.571	0.1095	-13	36
492.571	0.1018	-32	39
494.570	0.0963	-65	33
495.570	0.0987	-76	59
496.571	0.0976	-71	48
497.571	0.0998	-51	49

Table 3. Nodding and Precessional Model Parameters

Parameter	H α -	H α +	Adopted
N	47	54	...
t_{or} (HJD-2,451,000)	460.44	460.39	460.42 ± 0.04
ξ_0 ($^\circ$)	84.6	85.2	84.9 ± 0.5
$\Delta\xi$ ($^\circ$)	5.3	5.8	5.5 ± 0.5
r.m.s. (z)	0.008	0.011	...

Table 4. H α Stationary Emission Fits

Date (HJD-2,451,000)	W_λ (\AA)	FWHM (\AA)	V_{centroid} (km s^{-1})	V_{peak} (km s^{-1})
53.674	-342	16.0	204	233
55.677	-312	14.2	302	276
56.709	-376	14.7	255	280
57.721	-388	14.8	133	251
62.699	-88	15.1	291	173
354.740	-200	20.8	365	273
354.925	-282	21.1	367	277
355.738	-296	17.6	420	314
355.878	-299	17.4	383	321
356.813	-306	17.3	480	337
356.932	-301	16.5	483	341
357.769	-317	17.4	475	355
357.887	-306	17.1	449	370
359.747	-303	19.4	515	328
359.865	-282	18.8	488	345
360.697	-305	22.7	519	313
360.889	-298	23.7	493	313
361.895	-337	24.9	415	318
361.932	-324	25.3	384	314
363.716	-295	25.2	234	166
363.891	-260	24.2	282	196
364.921	-378	22.5	718	151
364.953	-245	22.4	533	172
395.869	-265	15.8	445	254
398.932	-216	13.5	323	229
399.890	-246	14.8	387	249
421.670	-105	12.4	141	182
421.726	-108	12.4	136	179
423.722	-213	13.1	237	182
424.642	-227	17.7	258	168

Table 4—Continued

Date (HJD-2,451,000)	W_λ (Å)	FWHM (Å)	V_{centroid} (km s ⁻¹)	V_{peak} (km s ⁻¹)
424.717	-286	17.6	343	179
425.688	-204	14.4	244	185
425.743	-223	13.8	284	177
426.632	-157	13.5	234	173
427.704	-177	13.2	246	146
428.617	-157	12.2	-4	57
428.677	-193	12.4	171	145
429.624	-171	13.4	98	102
429.675	-216	13.6	195	139
463.619	-336	15.1	163	168
463.674	-338	15.1	176	176
464.618	-246	15.3	158	147
464.669	-240	15.2	178	160
465.617	-226	15.5	119	119
465.674	-211	15.5	117	117
466.611	-208	16.1	24	69
466.660	-199	16.0	43	76
467.612	-205	15.1	49	65
467.672	-195	14.8	51	65
468.687	-202	14.6	74	60
491.644	-368	14.6	335	150
492.622	-377	15.1	126	129
493.612	-376	15.5	158	119
494.621	-379	16.7	159	111
495.623	-363	21.7	127	70
496.619	-329	26.5	-10	11
497.623	-255	26.0	28	52

Table 5. He I Stationary Emission Fits

Date (HJD-2,451,000)	W_λ (Å)	FWHM (Å)	V_{centroid} (km s ⁻¹)	V_{peak} (km s ⁻¹)
He I λ 5876				
355.738	-3.2	4.8	151	193
356.813	-4.6	11.0	65	205
359.747	-5.3	8.5	240	274
360.697	-4.6	9.2	157	219
362.839	-4.2	3.5	34	114
363.716	-2.9	5.0	53	71
364.921	-5.2	6.2	7	68
395.869	-8.8	8.4	259	263
399.890	-4.0	6.2	227	248
421.726	-4.1	6.2	139	209
423.722	-10.2	6.8	93	186
424.717	-8.9	10.0	104	194
425.743	-7.1	8.4	107	177
427.704	-6.9	9.3	22	125
428.677	-7.5	8.5	16	115
429.675	-11.5	9.1	80	164
463.674	-11.9	9.5	250	206
464.669	-7.5	10.6	207	183
491.644	-12.2	13.1	175	152
494.621	-7.7	12.1	196	145
495.623	-7.6	7.1	101	90
496.619	-7.5	7.7	100	111
497.623	-5.2	8.0	205	178
He I λ 6678				
53.674	-8.3	6.7	303	226
55.677	-8.2	8.0	251	237

Table 5—Continued

Date (HJD-2,451,000)	W_λ (Å)	FWHM (Å)	V_{centroid} (km s ⁻¹)	V_{peak} (km s ⁻¹)
56.709	-10.1	9.8	307	241
57.721	-10.4	10.3	316	234
354.740	-1.7	6.0	210	219
362.839	-8.4	18.5	66	-3
363.716	-4.9	9.4	40	85
363.891	-3.2	8.0	85	91
364.921	-6.4	9.0	96	86
364.953	-4.7	8.4	130	112
421.670	-2.7	4.2	45	199
424.642	-5.6	8.6	-52	192
424.717	-1.8	4.8	123	199
425.688	-4.3	5.7	53	162
425.743	-2.5	4.8	139	178
426.632	-3.3	9.7	77	180
427.704	-2.8	10.0	14	116
428.617	-4.3	10.3	-79	96
428.677	-4.8	10.8	-6	133
429.624	-7.5	6.7	-99	126
429.675	-4.8	6.6	-6	137
463.674	-9.6	9.1	178	172
464.618	-7.1	10.9	81	89
464.669	-7.0	11.1	91	86
465.617	-7.4	11.8	-24	17
465.674	-6.9	11.6	-31	13
466.611	-6.7	9.9	-82	-32
466.660	-6.5	9.7	-82	-37
467.612	-5.9	9.4	-41	-22
467.672	-5.7	9.3	-54	-18
468.687	-5.3	10.0	-73	-28
491.599	-6.0	11.4	99	119

Table 5—Continued

Date (HJD-2,451,000)	W_λ (Å)	FWHM (Å)	V_{centroid} (km s ⁻¹)	V_{peak} (km s ⁻¹)
493.612	-5.2	11.3	66	44
494.570	-4.2	11.0	135	81
494.621	-4.1	8.2	108	66
495.570	-5.5	9.4	60	59
495.623	-5.2	8.5	74	66
496.571	-5.6	8.9	70	59
496.619	-5.2	9.3	41	62
497.571	-4.7	8.4	54	68
497.623	-4.9	8.5	89	83
He I λ 7065				
355.878	-16.2	11.0	464	301
356.932	-10.5	11.0	368	328
357.887	-12.0	12.9	217	319
359.865	-12.8	11.2	531	291
360.889	-10.6	12.6	487	246
361.932	-10.0	14.2	138	225
421.670	-2.7	5.8	114	206
424.642	-14.1	10.6	-128	186
425.688	-7.7	8.6	-49	177
426.632	-6.1	11.0	-56	158
428.617	-7.2	10.3	-130	95
429.624	-9.9	8.2	-92	124
463.619	-16.4	11.5	124	176
464.618	-10.1	12.5	151	158
465.617	-9.8	13.0	100	114
466.611	-9.3	13.5	61	49
467.612	-8.5	12.6	62	36
468.687	-9.2	12.7	-5	3

Table 5—Continued

Date (HJD-2,451,000)	W_λ (\AA)	FWHM (\AA)	V_{centroid} (km s^{-1})	V_{peak} (km s^{-1})
494.570	-6.7	13.5	120	79
495.570	-9.3	12.2	253	90
496.571	-9.9	10.6	188	79
497.571	-7.5	9.8	167	117

Table 6. He I Stationary Emission Peak Radial Velocity Fits

Element	H α	He I λ 5876	He I λ 6678	He I λ 7065
K (km s $^{-1}$)	67 (5)	59 (6)	60 (5)	71 (5)
ϕ (max.)	0.04 (3)	0.01 (5)	−0.03 (3)	−0.01 (3)
V_1 (km s $^{-1}$)	219	...	194	...
V_2 (km s $^{-1}$)	281	167	143	252
V_3 (km s $^{-1}$)	206	225
V_4 (km s $^{-1}$)	152	163	163	157
V_5 (km s $^{-1}$)	113	154	31	97
V_6 (km s $^{-1}$)	130	170	112	148
r.m.s. (km s $^{-1}$)	27	31	21	16

Table 7. UV Flux Limits (10^{-18} erg cm $^{-2}$ s $^{-1}$ Å $^{-1}$)

Range (Å)	$\langle \lambda \rangle$ (Å)	n	F_λ	σ_μ	$F_\lambda + 2\sigma_\mu$
1155 – 1185	1170.08	52	0.8	3.9	8.6
1195 – 1235	1215.05	68	3.5	14.8	33.0
1250 – 1275	1262.65	43	–1.3	1.2	2.5
1285 – 1320	1302.65	60	1.6	1.6	4.8
1340 – 1380	1359.88	68	3.3	1.4	6.1
1400 – 1450	1425.00	85	0.8	0.6	2.1
1450 – 1500	1474.93	86	0.6	0.8	2.2
1500 – 1550	1525.16	86	1.1	0.9	2.8
1550 – 1600	1575.09	85	1.8	1.2	4.2

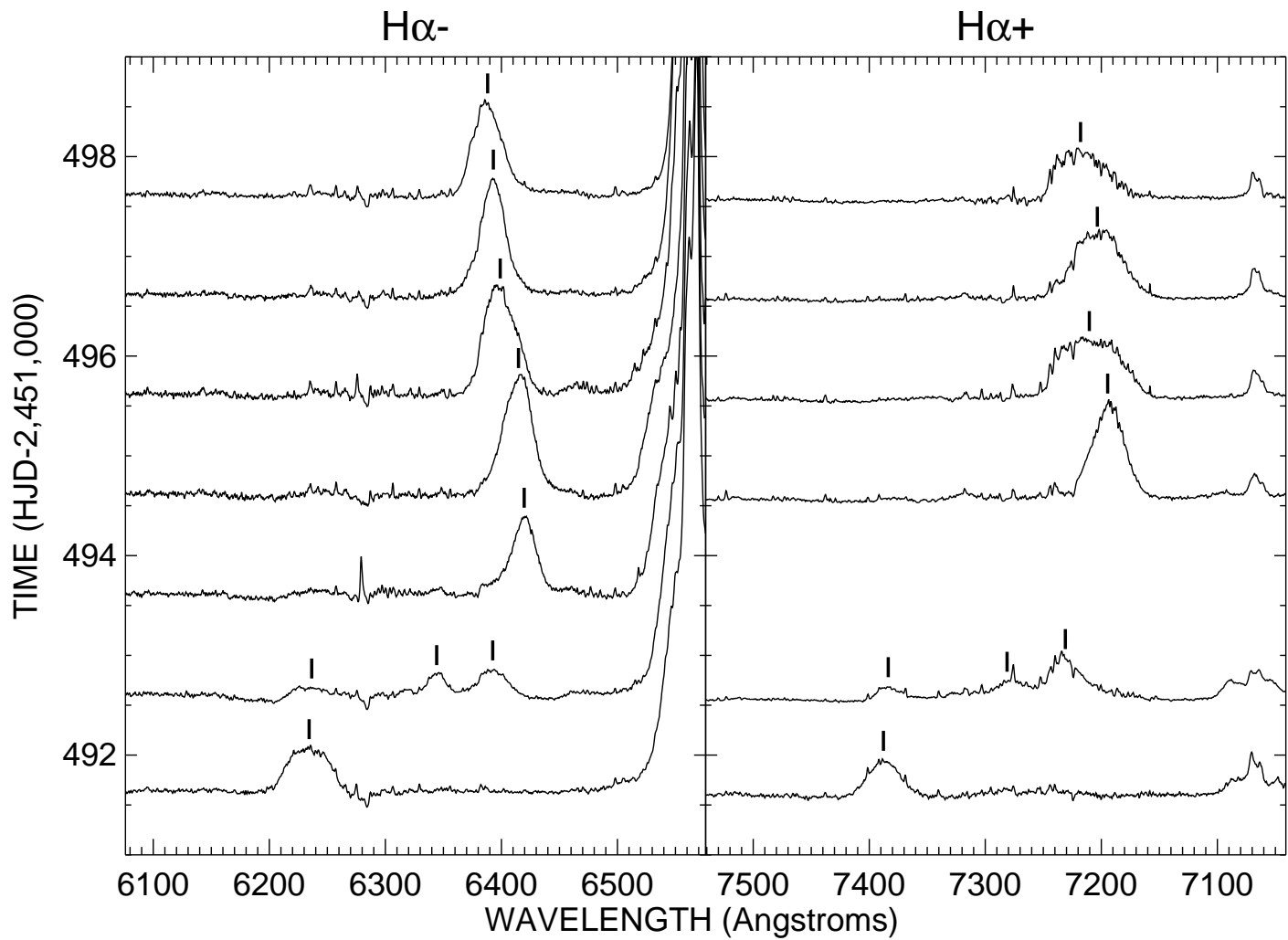


Fig. 1.—

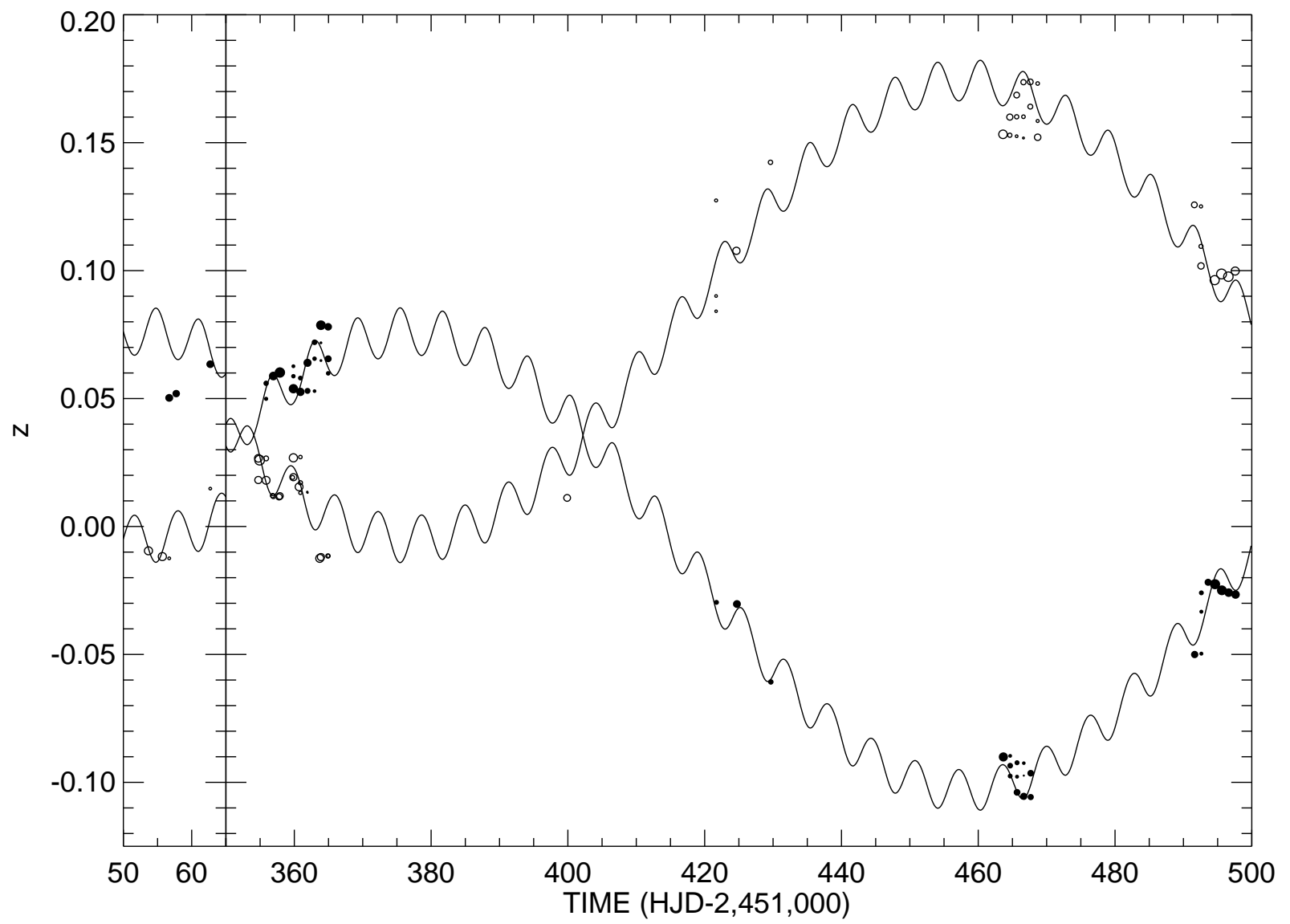


Fig. 2.—

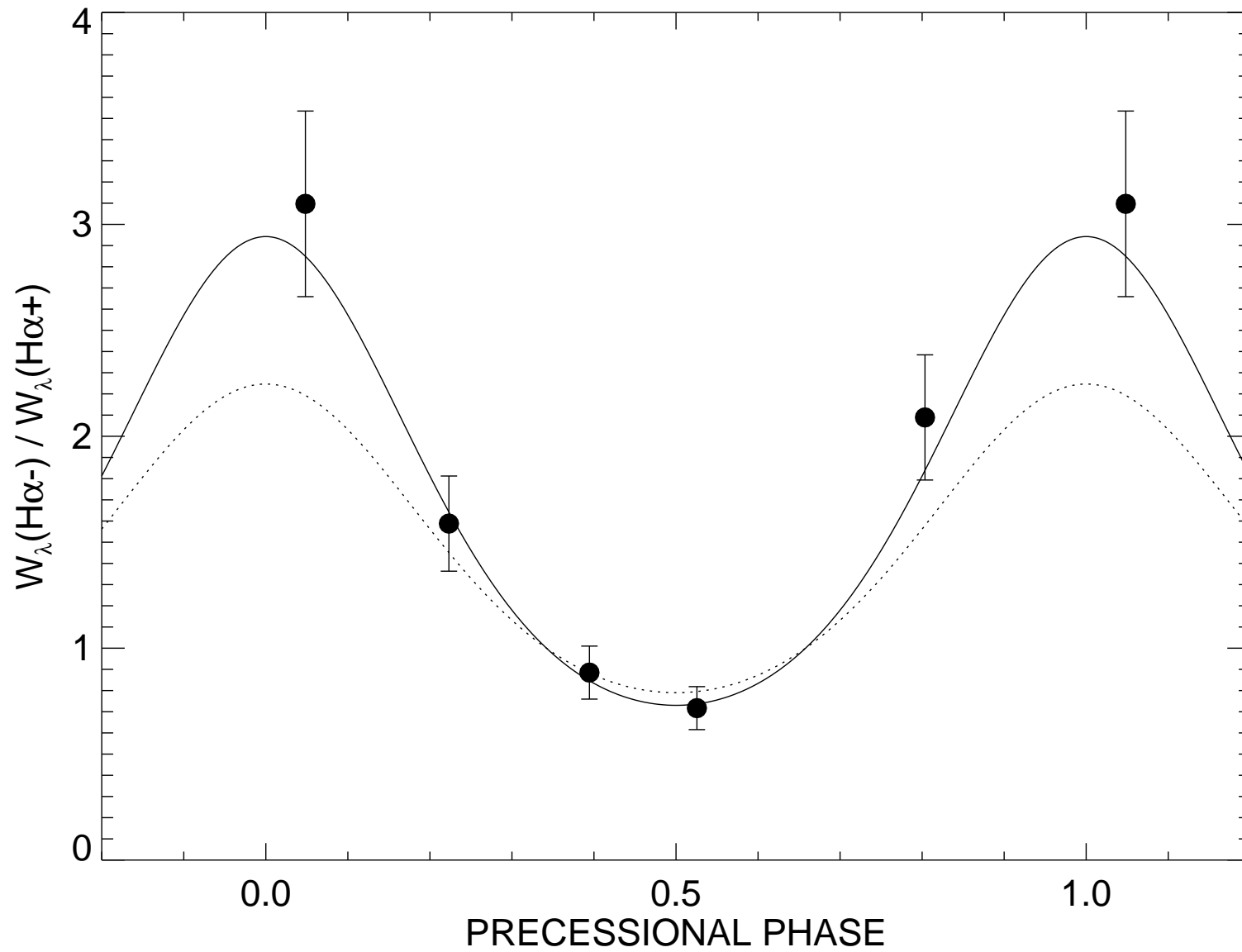


Fig. 3.—

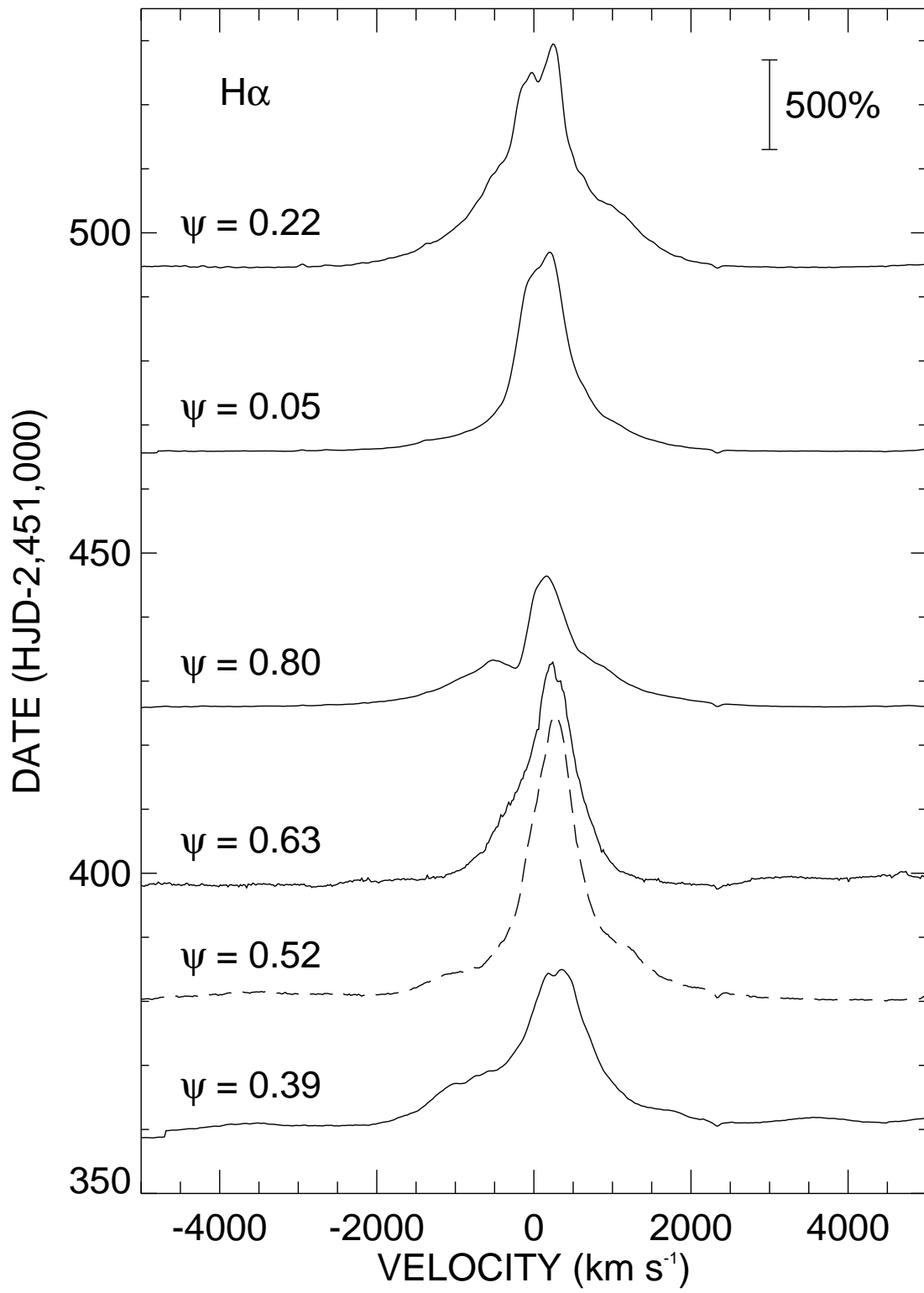


Fig. 4.—

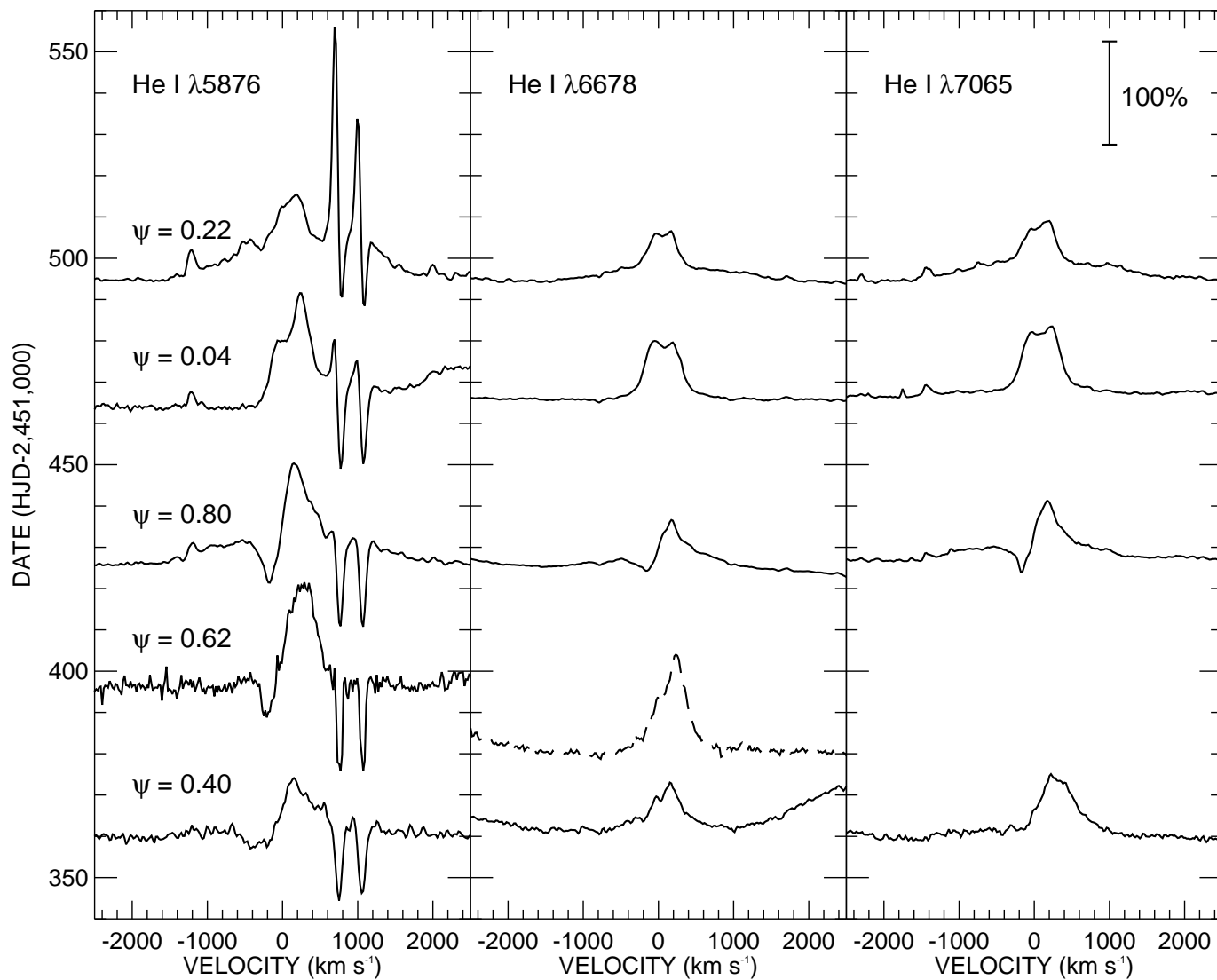


Fig. 5.—

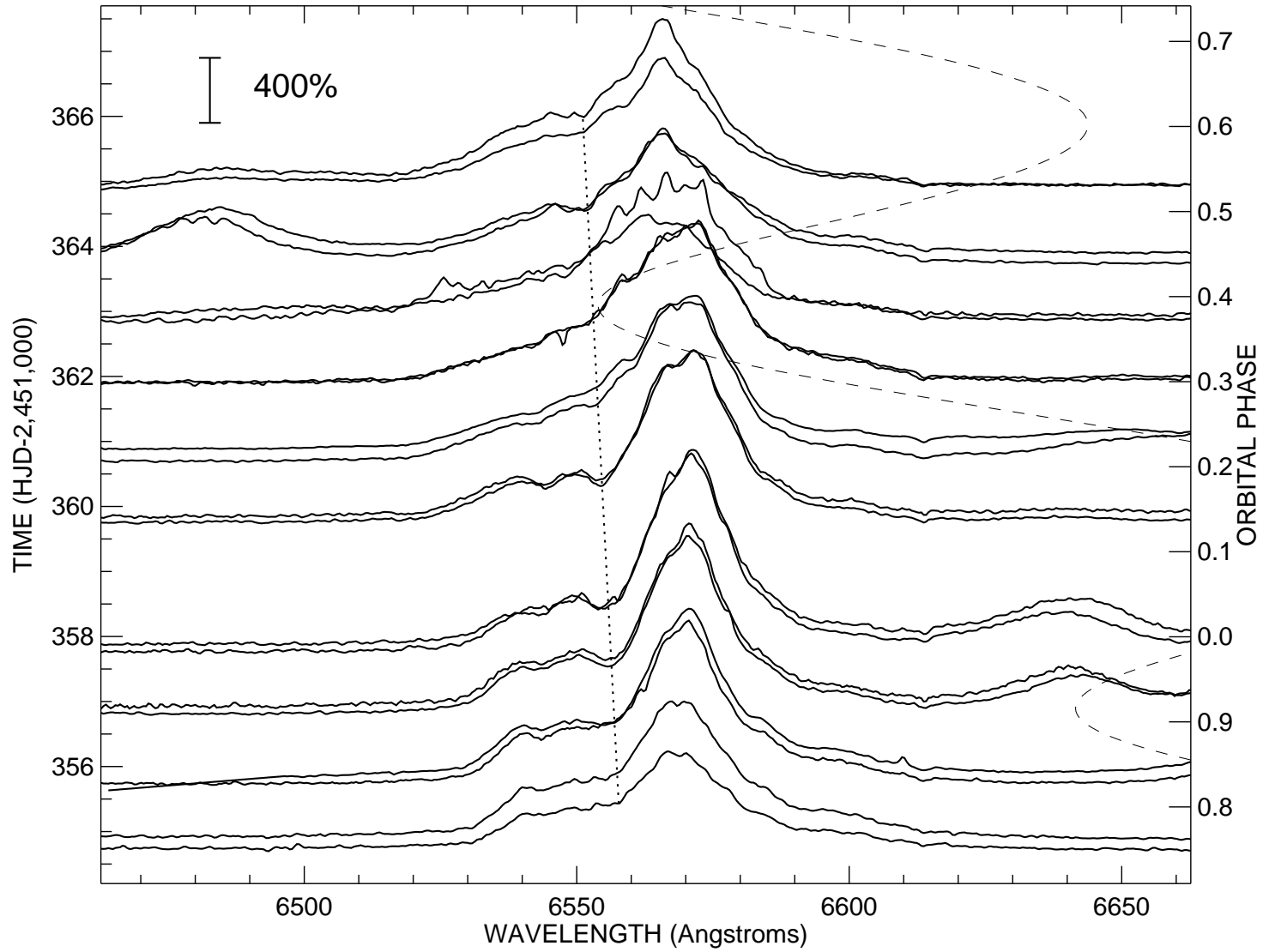


Fig. 6.—

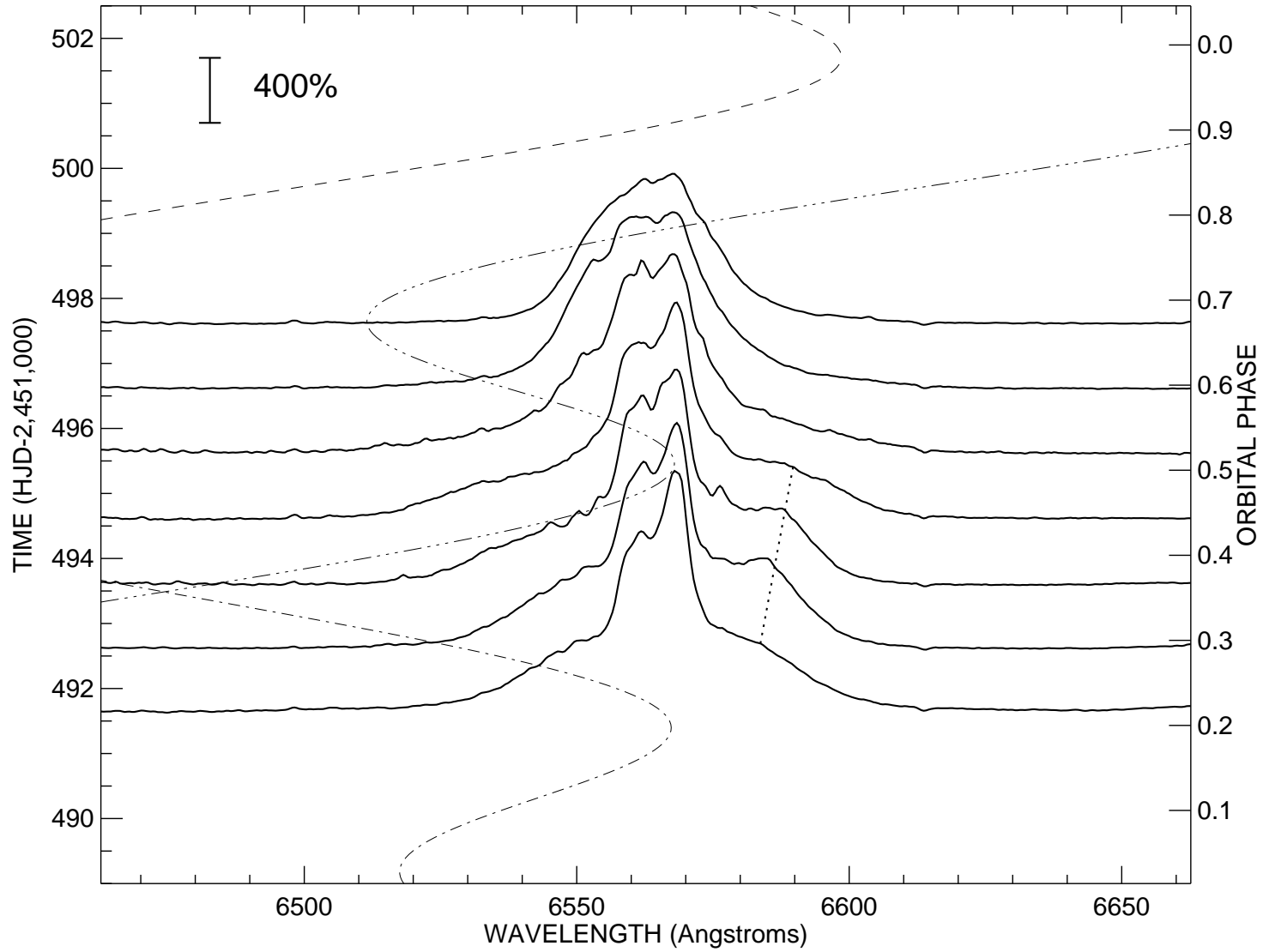


Fig. 7.—

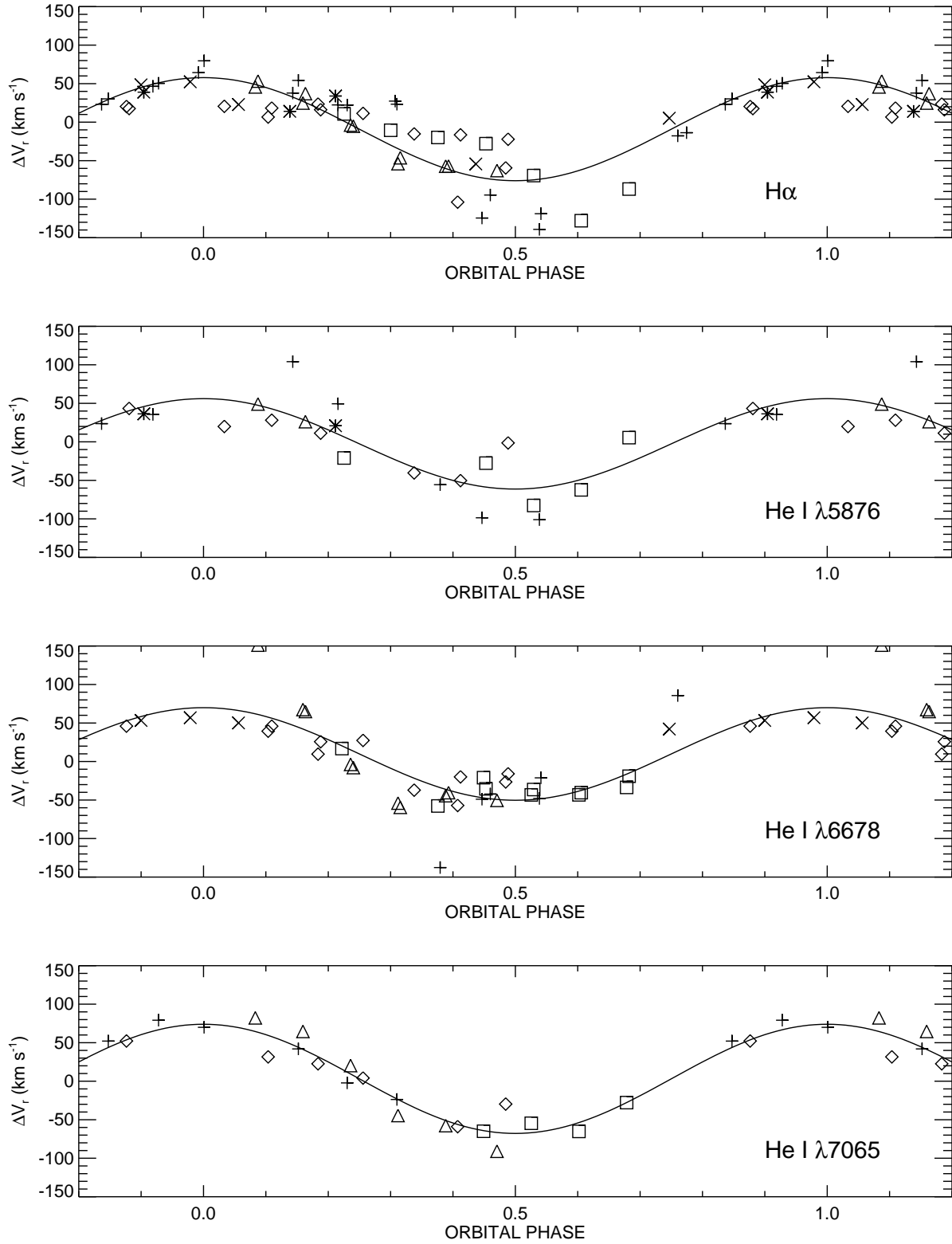


Fig. 8.—

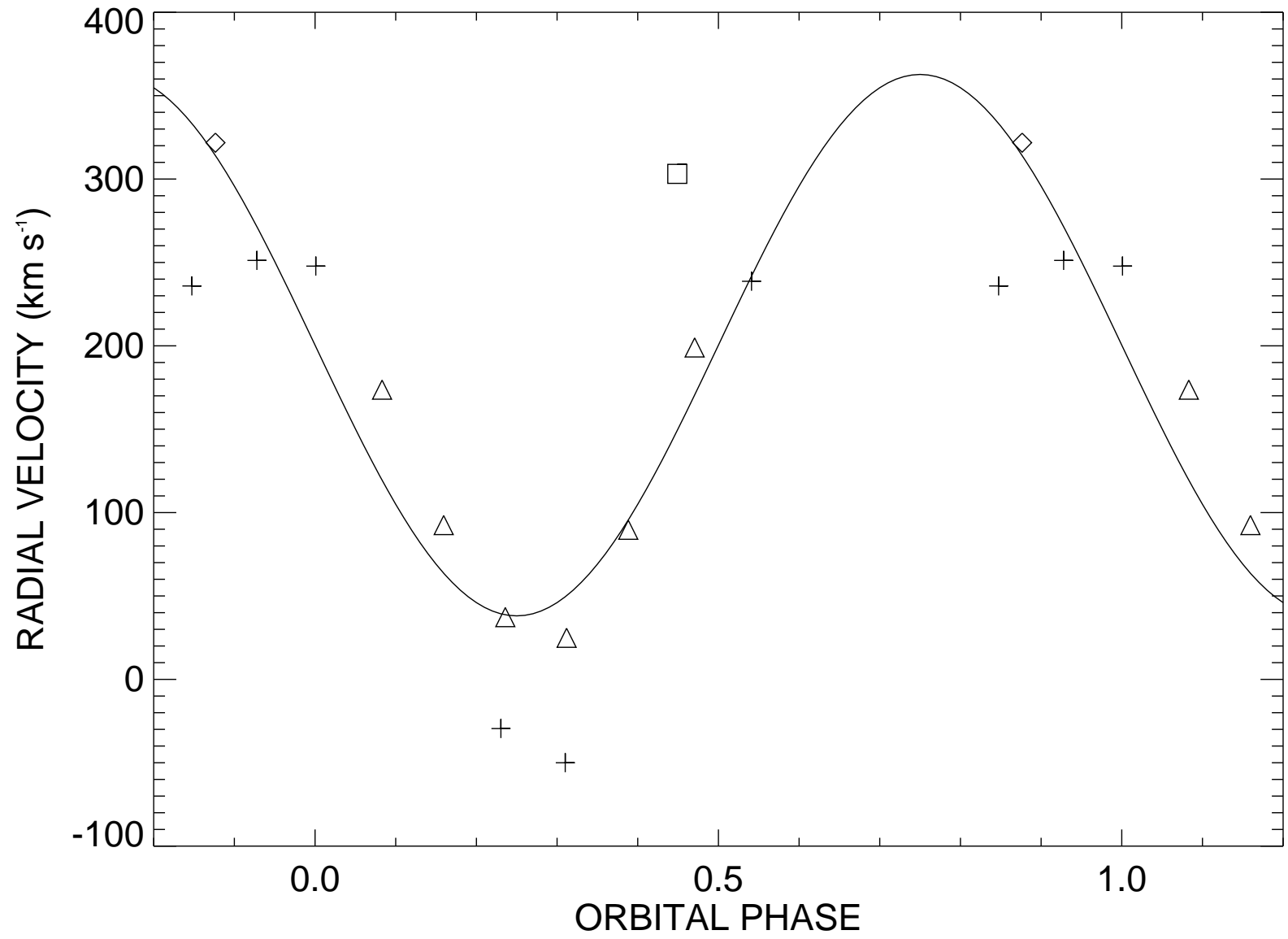


Fig. 9.—

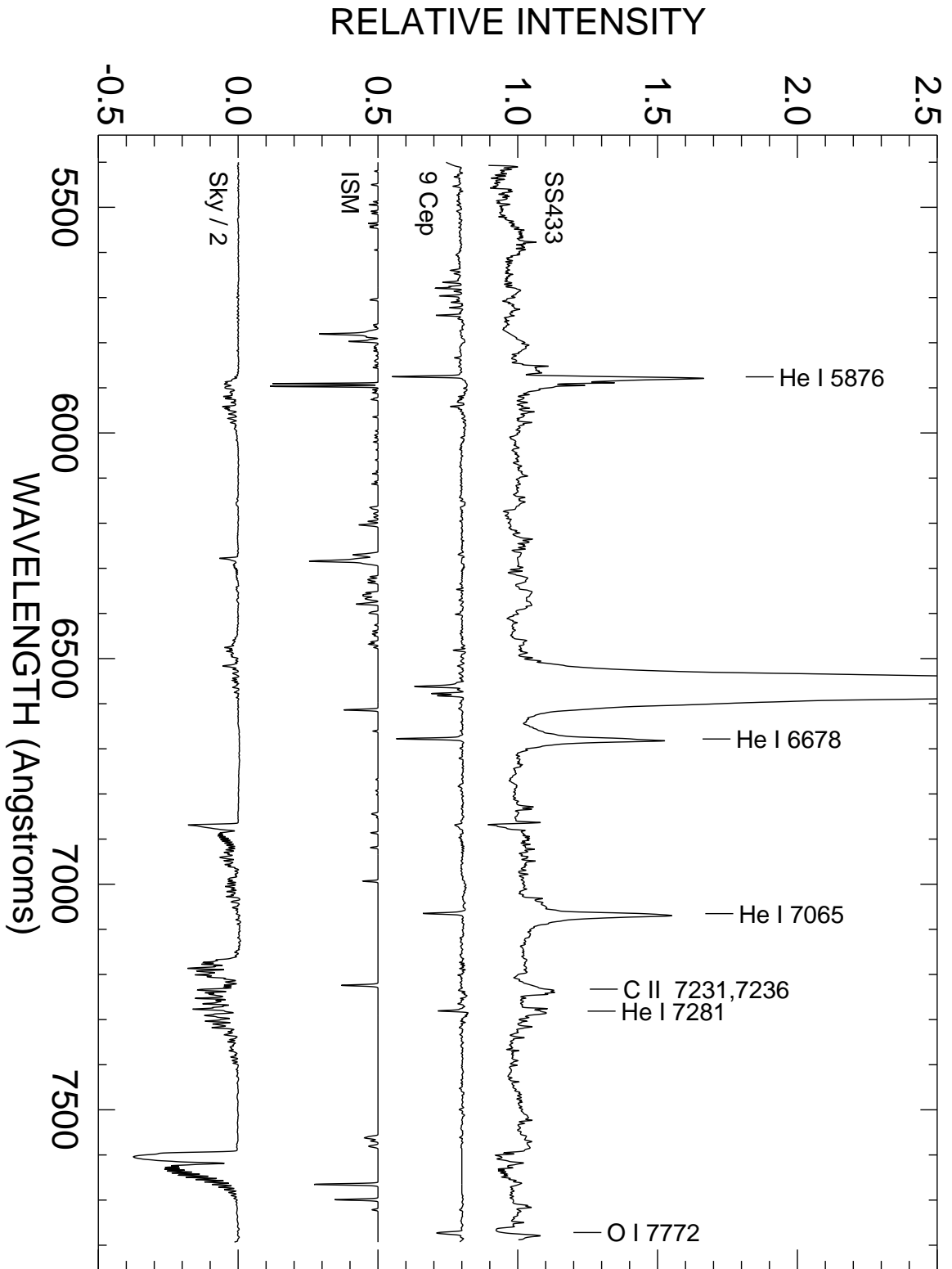


Fig. 10.—

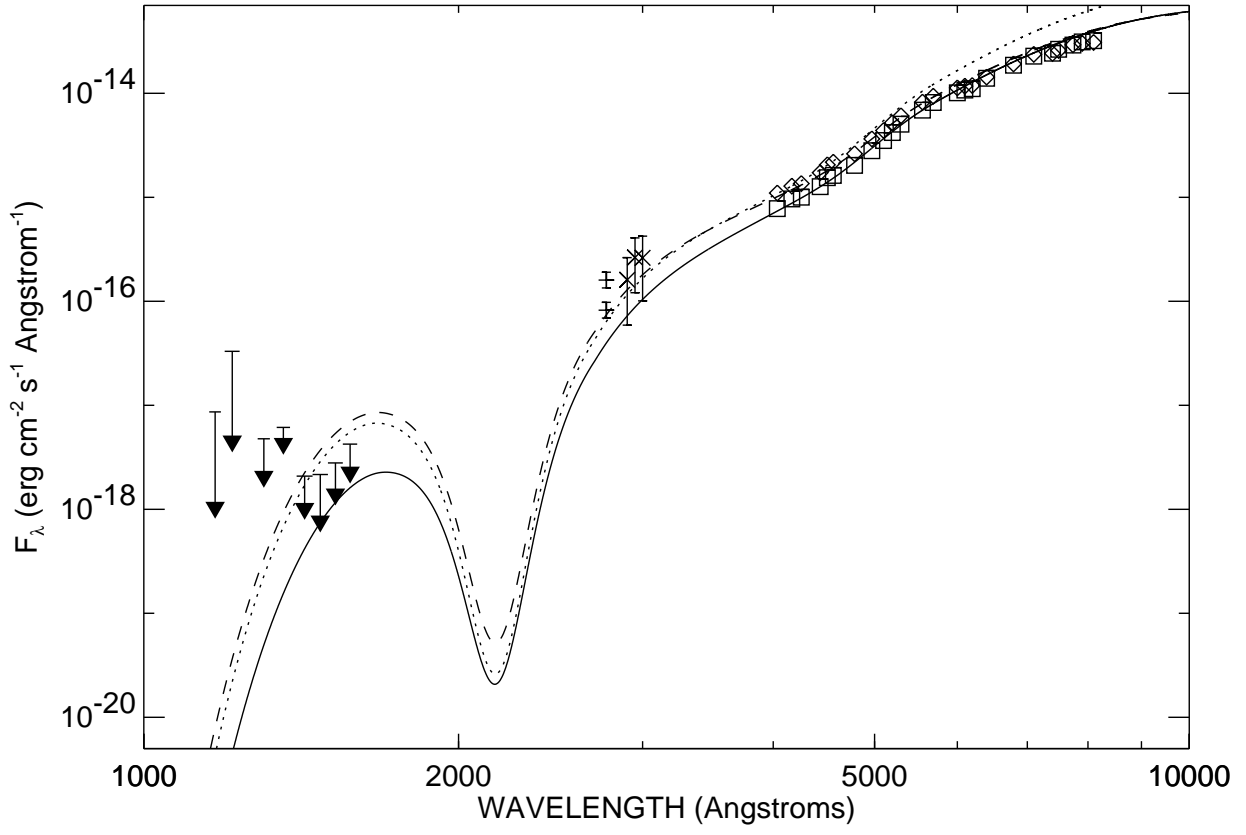


Fig. 11.—

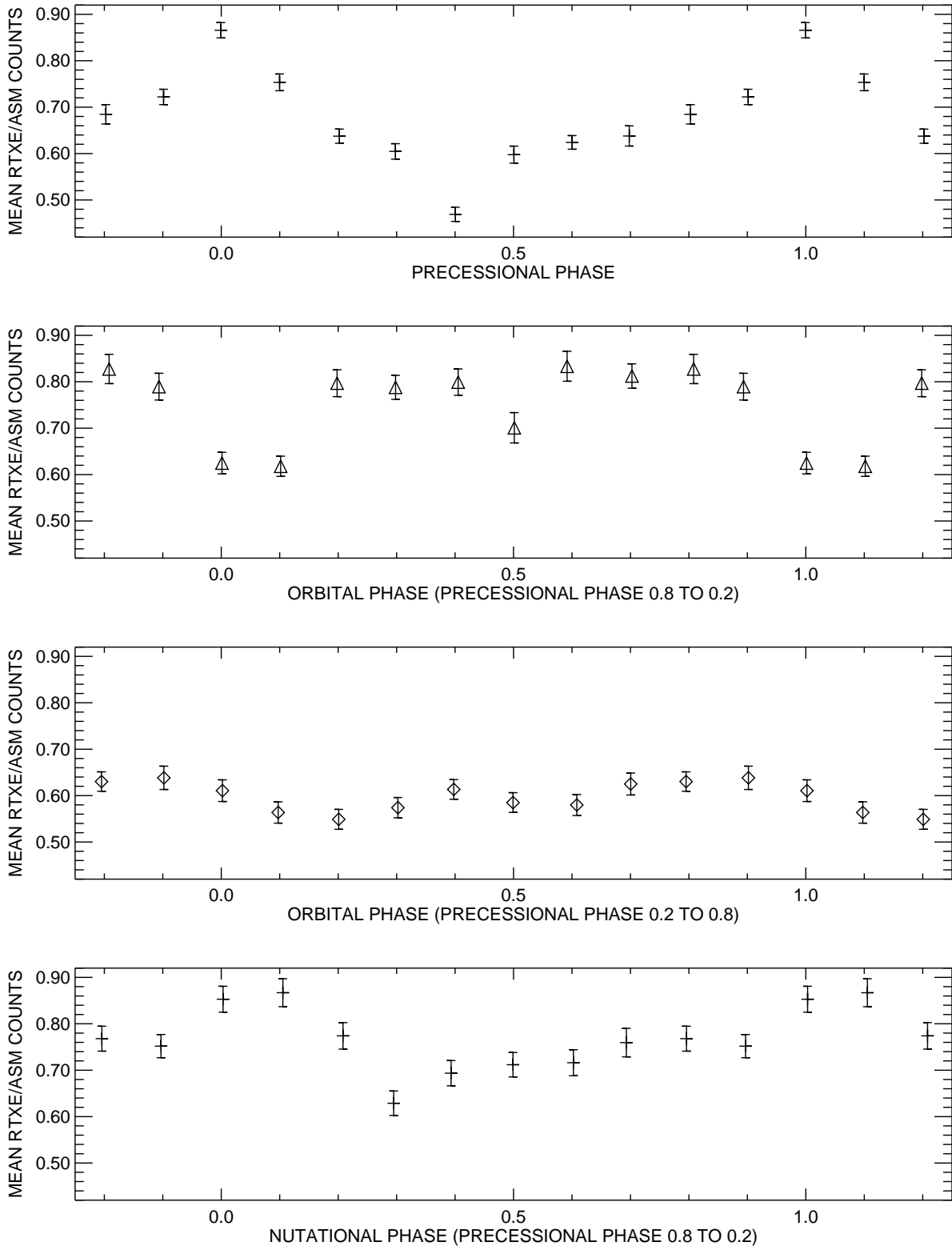


Fig. 12.—

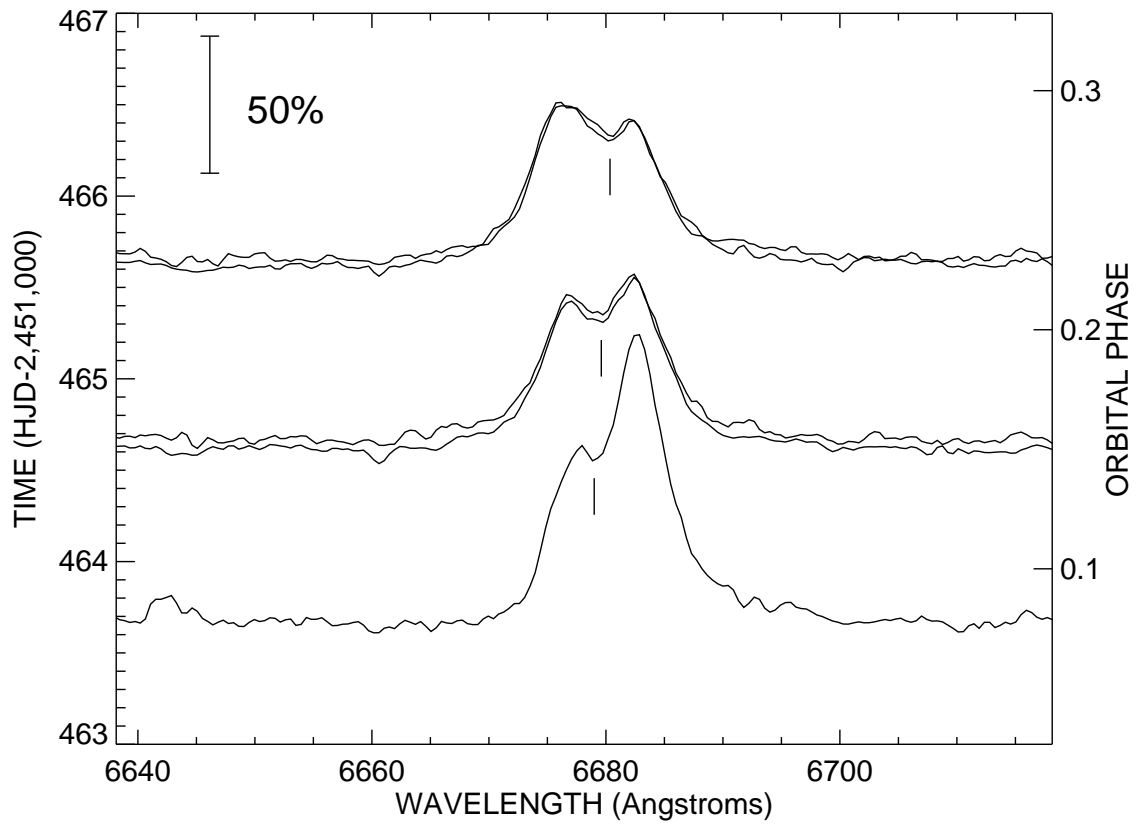


Fig. 13.—